SEISMIC IMAGING OF ANISOTROPIC DOMAINS: PHYSICAL MODELING AND A BAKKEN SHALE FIELD CASE

A Thesis

Presented to

the Department of Earth and Atmospheric Sciences

University of Houston

In Partial Fulfillment

of the Requirements for the Degree

Master of Science

By

Omoboya Olabode Kingsley

December 2011

SEISMIC IMAGING OF ANISOTROPIC DOMAINS: PHYSICAL MODELING AND A BAKKEN SHALE FIELD CASE

Omoboya Olabode Kingsley

APPROVED:

Dr. Robert R Stewart, Chairman (University of Houston)

Dr. Christopher Liner, Committee Member (University of Houston)

Dr. Robert Wiley, Committee Member (University of Houston)

Dr. Robert Horine, Committee Member (Hess Corporation)

Acknowledgements

I would like to thank Dr. Robert Stewart for giving me the opportunity to participate in remarkable research at the Allied Geophysical Laboratories and for permission to present this work. Dr. Chris Liner and Dr. Bob Wiley are also thanked for providing advice on seismic processing and physical modeling respectively. Thanks to Dr. Robert Horine of the Hess Corporation for providing the field data that formed the basis of this research. I am grateful to Dr. Samik Sil of ConocoPhillips (Houston) and Dr. Mark Willis, formerly of ConocoPhillips, for their enthusiastic technical and financial support of the fractured glass model work. I also acknowledge Paradigm Geophysical and GEDCO (Geophysical Exploration and Development Corporation) for software support.

SEISMIC IMAGING OF ANISOTROPIC DOMAINS: PHYSICAL MODELING AND A BAKKEN SHALE FIELD CASE

An Abstract of a Thesis

Presented to

the Department of Earth and Atmospheric Sciences

University of Houston

In Partial Fulfillment

of the Requirements for the Degree

Master of Science

By

Omoboya Olabode Kingsley

December 2011

Abstract

One of the major aspirations of geophysical research is to accurately predict the seismic response of fractured regions within the subsurface. This research project details a series of physical modeling experiments combined with analyzed field acquired data to help achieve this aim. This thesis explores the ultrasonic response of laser-made fracture models with different fracture orientation and geometry that were designed to mimic plausible fracture patterns of the Bakken Formation of the Williston Basin. Since the different units of the Bakken Formation are sometimes believed to effectively possess orthorhombic symmetry, physical modeling experiments were conducted on intrinsically orthotropic phenolic models. In this experiment, uniaxial stress was tested against anisotropic parameters. This study also explored the geologic phenomenon that dominates the contortion of anisotropy under different stress tenure. These experimental observations were compared to processed Red Sky 2D data. Results from the laser-etched fracture models show that residual eta values are highest at seamlessly horizontally layered (VTI) models. We relate these results directly to residual curvatures observed in the Greenhorn and Bakken Formations in the Red Sky survey. From the phenolic model experiments, we can infer that polar anisotropic symmetry dominates the character of anisotropy as overburden pressure increases.

Table of Contents

List of Figures

Objective

The broad objective of this research project is to understand the seismic response to fractures. The individual experiments that contributed to this report were initially independent experiments or studies aimed mostly at understanding the anisotropic response of different earth models. Phenolic models were used to simulate intrinsically anisotropic layered rocks under pressure from overlying sediments. The laser-etched glass models were to simulate different plausible fracture patterns and orientation in the earth. In the Red Sky survey, an attempt was made at extracting seismic response attributable to better productivity in the Bakken Formation.

This thesis is an attempt at integrating all individual studies and finding a relationship between laboratory measurements and field data. The aims were to model geological settings in the field survey area in the lab and analyze processed field data for similarity.

Introduction

Although considerable effort has been dedicated to numerically and physically imaging subsurface fractures, a great deal of work still needs to be done.

This project attempts to image fractures of different dimensions with a range of tools. A seismic response is a superposition of transmitted, reflected, and scattered signals and this project aims at extracting that response due to fracture swarms from both reflected and scattered seismic energy. Fracture spacing can range from a few millimeters to hundreds of meters. Seismic response can also vary depending on the ratio of fracture size to seismic wavelength. In one approach, a large seismic wavelength is considered relative to smaller fracture dimension, in which case, we expect an effective seismic response and fracture-induced anisotropy. Different theories of seismic wave propagation in fractured media (effective medium theories) have been proposed by Hudson (1981), Hudson and Boore (1980), Hudson and Crampin (1996), Schoenberg (1980, 1983) and Thomsen (1986). Another approach considers the scenario in which seismic wavelength is similar to or lesser than fracture size. In this situation, there is elastic scattering. Analysis of the resultant seismic coda can provide invaluable information about fracture orientation and spacing. Seismic coda represents the seismic energy following the direct reflected wavefront (Aki, 1969). Theories of scattered wave energy propagation have been suggested by Aki (1969) and Aki

and Chouet (1975). A variety of techniques have also been used in the past to extract orientation and spacing of fractures; the scattering index method by Willis et al. (2006) is based on the fact that stacks of data acquired parallel to the direction of fractures retain the scattered seismic energy and that the reverse is the case for orthogonal fracture sets. Grandi et al. (2007) offered FK analysis as a way to estimate fracture spacing.

Each chapter here details an independent set of experiments and different analysis stages on field data. Most are physical modeling experiments with the addition of a field seismic data example. In a seismic physical modeling experiment, an attempt is made at estimating the seismic response of a geologic model by measuring the reflected or transmitted wavefield over the scaled model (Ebrom and McDonald, 1994). Among the advantages of physical modeling is its cost effectiveness compared to field work. It is also assumed with a fair degree of accuracy that the physics of elastic propagation in a scaled physical model is the same as that in the real world.

The first chapter presents different physical modeling experiments that were carried out on laser-etched fracture models to estimate the amplitude and velocity response of fractures. Seismic non-hyperbolic moveout experiments were also carried out on glass models to help understand which kind of media perpetuates the highest and most reliable residual eta values.

Chapter 2 presents experiments on anisotropy, specifically orthorhombic anisotropy. Orthorhombic anisotropy occurs in a sedimentary basin when there are vertical fractures combined with a background polar anisotropy (VTI). As a result, it is the simplest realistic symmetry for any geophysical problem (Schoenberg and Sayers, 1995). Anisotropic parameters and stiffness coefficients were examined in different stress regimes. This would be geologically analogous to layered sedimentary rocks with vertical fractures under the influence of pressure from overlying sediments.

Chapter 3 discusses the survey location and geology of the survey area. Previous studies by Ye at al. (2010) and Jones and Wang, (1981) were discussed. Introductory details about the Red Sky seismic and well surveys are presented. The seismic and well surveys were courtesy of the Hess Corporation and additional well information was provided by the North Dakota Industrial Commission.

Chapter 4 covers all the seismic processing details of the Red Sky field data. Geometry and QC, deconvolution and general noise attenuation techniques were mentioned. Preliminary velocity analysis and migration are also included.

In chapter 5 presents the analysis of the Red Sky field data and compares them to results obtained from physical modeling experiments. The field data were analyzed for anisotropic parameters and attempts were made at comparing formations with high shale volume to areas of high residual eta. The same seismic

non-hyperbolic moveout was also compared to previously measured stiffness coefficients from core shale samples.

Conclusions are stated in chapter 6.

Appendix A explains the fundamentals of acoustic scattering and seismic anisotropy. It gives a theoretical background of all the techniques used in this project. Different anisotropic symmetries are detailed, from simple polar anisotropy to more advanced orthorhombic models. Wave propagation basics of seismic coda are also presented.

Chapter 1

Experimental investigation of ultrasonic response in laser-etched fracture models

1.1 Introduction

This chapter details a series of experiments performed on fracture-embedded glass models with the aim of extracting the seismic response of these fracture corridors. This research project was originally sponsored by ConocoPhillips. Primarily, laser-etched fractured glass models are used as physical models with an array of surface seismic, transmission, and ultrasonic measurements being taken on these models. All experiments were performed at the Allied Geophysical Laboratories (AGL) at the University of Houston. Three types of experiments that were performed: 1) Ultrasonic measurements on fractured glass models at the AGL's non-destructive testing facility; 2) Transmission (3D) measurements in the acoustic (or marine) physical modeling facility; and 3) surface seismic measurements at the elastic (or land) physical modeling facility.

Preliminary results show that the use of these laser-etched fracture models to investigate fracture swarms is highly encouraging. Compressional and shear wave velocities reduce marginally when travelling perpendicular to fractures. However, seismic amplitudes tend to increase when propagating through this fracture, which is an indicator for increased coda signature. In the reflection experiments, we found residual moveout to be unstable on encountering non-VTI symmetry.

1.2 Models, instrumentation, and experimental methods

1.2.1 Marine system

At the heart of the AGL marine system is a 3m x 2m x 1.5m acoustic physical modeling tank. This tank is equipped with a positioning system (to help locate relative positions of source and receiver) and it is attached to a measuring and recording device. The recording system runs on a National Instruments LABVIEW application. This system supports a maximum of 8 sources and 16 receivers (simultaneously). The marine system is used to simulate field marine and OBC experiments, as well as simultaneous source experiments. Figure 1.1 is a snapshot of the AGL marine tank. In a marine experiment, spherical and pin transducers are used to carry out experiments.

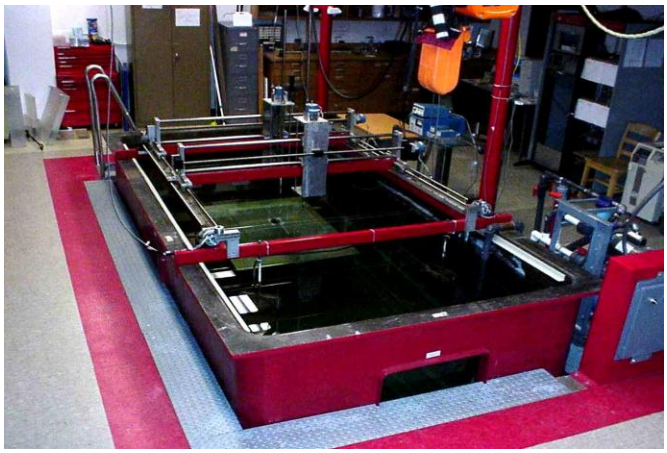

Figure 1.1. AGL's 3m X 2m X 1.5m marine/acoustic physical modeling system (Photograph by AGL personnel).

1.2.2 Land system

The AGL land system supports a maximum of 2 sources and 4 receivers (simultaneously). National Instrument's LABVIEW is also used for acquisition, positioning and recording. Flat-faced transducers are used mostly in land experiments and there is also the need for a coupling device such as honey, oils, etc. Figure 1.2 shows the land system during an experiment with a flat-faced transducer on a glass model.

1.2.3 Ultrasonic system

The ultrasonic measurement system consists of a series of non-destructive testing devices comprised of a 50 MHz digital oscilloscope with a travel time accuracy of 0.02 μs, a 1 MHz (5077) pulsar receiver and a host of other add-ons for optimum ultrasonic testing and measurement.

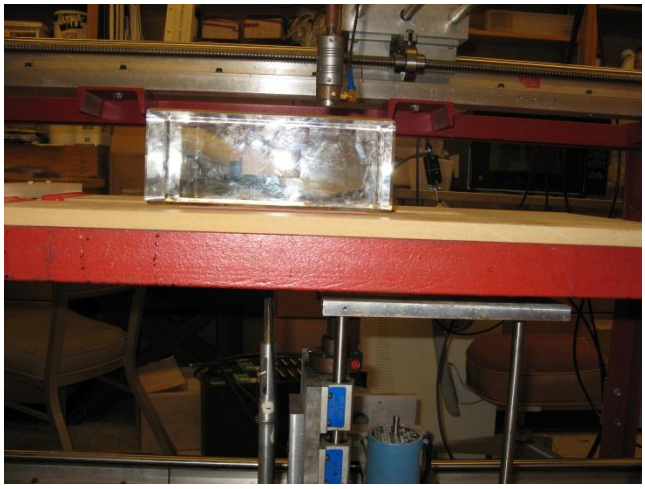

Figure 1.2. AGL's land physical modeling system showing a transducer and a glass model.

1.2.4 Transducers

The AGL boasts of an array of transducers, from 30 KHz pin transducers to 5MHz contact transducers, all utilized differently in individual experiments. Spherical transducers are most commonly used in the marine system, while shear wave and flat-faced contact transducers are used in the land system.

Figures 1.3, 1.4, 1.5, and 1.6 shows examples of ultrasonic transducers used in the experiments reported in this chapter.

Figure 1.3. Snapshot of a 300 KHz marine spherical transducer (Photograph by AGL personnel).

Figure 1.4. Snapshot of a 3C contact transducer (Photograph by Robert Wiley).

Figure 1.5. Snapshot of shear transducers (Photograph by AGL personnel).

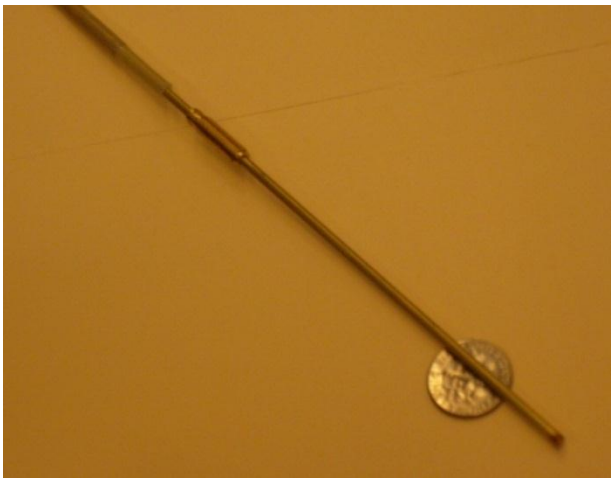

Figure 1.6. Snapshot of piezopins or pin transducers (Photograph by AGL personnel).

1.2.5 Models

A total of 5 glass (fracture) models were used in this research project. The models ranged in fracture orientation and geometry. There was also a blank glass block for the purpose of calibration. Fracture geometry is often made by laser etching inside such blocks. These fractured blocks were labeled C1, C3, C4, C9, and C10 with C3 being the blank glass model. Model C4 developed large cracks along one of its laser-etched fault planes during transport. The appearance of these seemingly unwanted cracks later proved invaluable to understanding how the laser-etched fractures were designed and to a better understanding of how fractures work. All the glass blocks were 21cm x 15cm x 8cm in dimension; fracture orientation and geometry, however, vary significantly from block to block. A schematics of all glass models is shown in Figure 1.7.

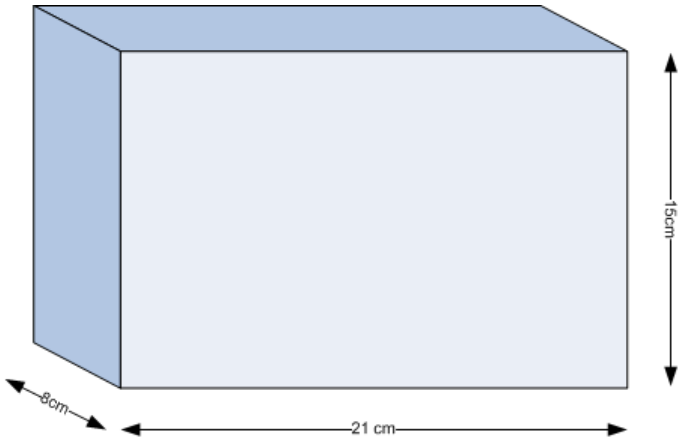

Figure 1.7. Schematic diagram of a typical glass model.

Models C1 and C4 were the major objects for the ultrasonic testing carried out for this report. Model C1 is made up of several “hair thin” vertical fracture veins each about 1mm apart. Figure 1.8 is a snapshot of Model C1. The dimension of the laser inclusion is 26 x 48 x 48 mm, as shown in the schematic of Model C1 in Figure 1.9.

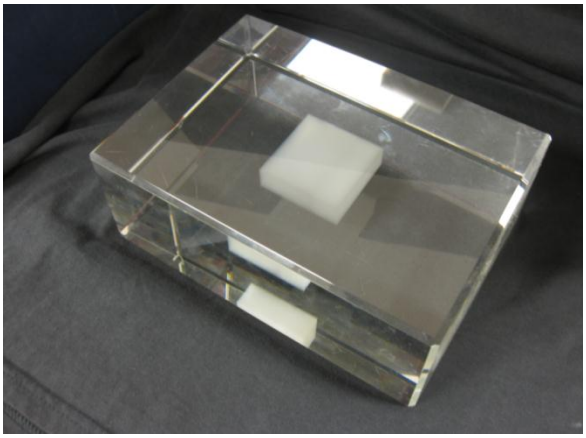

Figure 1.8. Snapshot of Model C1.

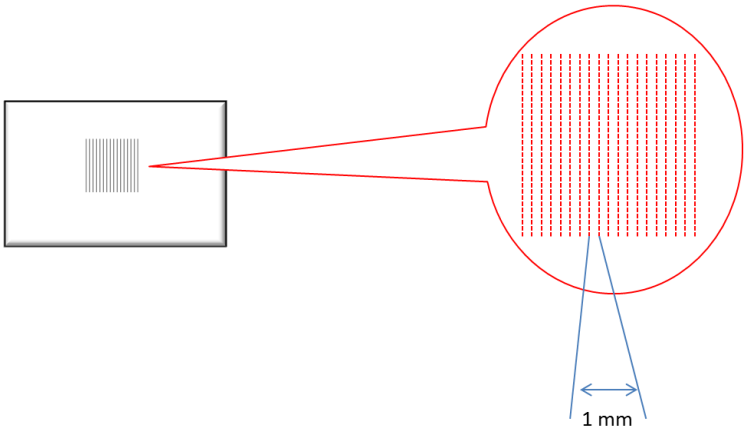

Figure 1.9. Schematic diagram of Model C1.

Model C4 had six major vertical fracture sets with 60 smaller fracture veins (HTI symmetry). It was a hybrid of Model C1. Figure 1.10a is a snapshot of Model C4, and Figure 1.10b is a zoom on the laser-etched fractures on the model. The dimension of the laser inclusion in Model C4 is once again 26 x 48 x 48 mm and a schematic is shown in Figure 1.11.

Model C3 was the blank glass model; it served as the calibration model. This model was used in all three types of experiments (ultrasonic, transmission and surface). Figure 1.12 shows a snapshot of Model C3.

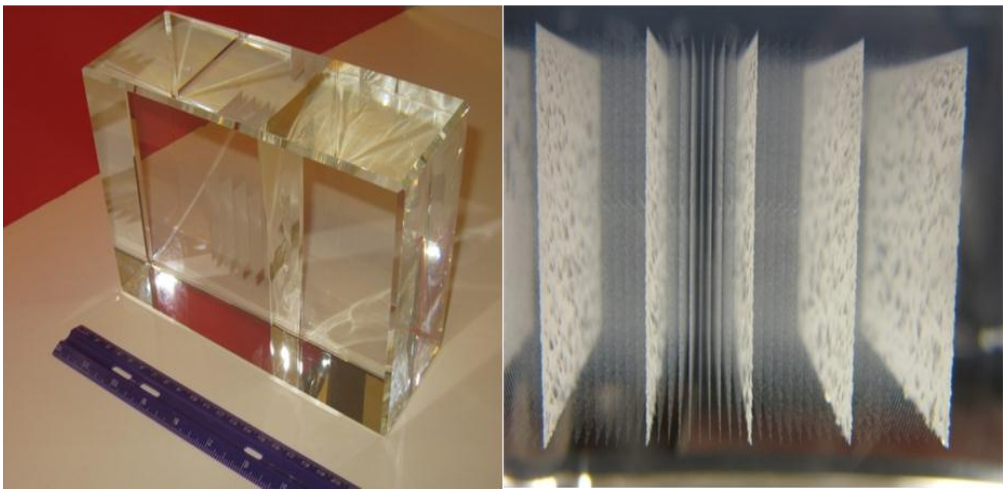

Figure 1.10. Model C4. a) snapshot of model C4; b) zoom on laser-etched fractures on Model C4 (Photograph by Nikolay Dyaur).

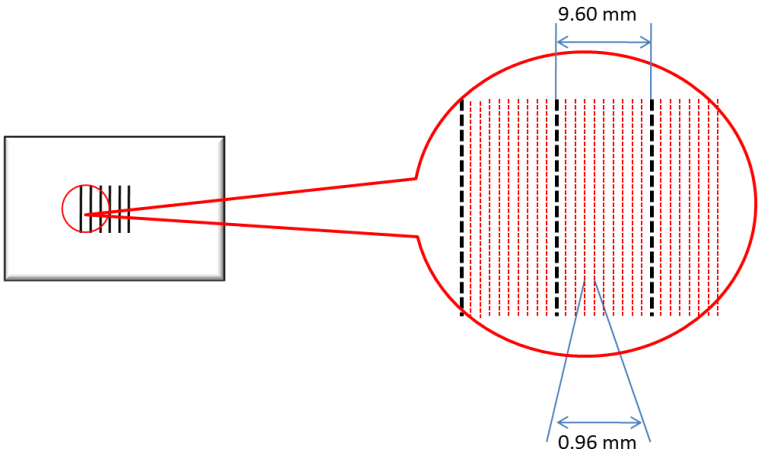

Figure 1.11. Schematic diagram of Model C4.

Figure 1.12. Snapshot of Model C3.

Models C9 and C10 were used only for surface measurements, specifically, for anisotropic (non-hyperbolic moveout) measurements. Fig 1.13 shows snapshots of both Models C9 and C10.

Figure 1.13. Snapshot of Models: a) C9 and b) C10.

1.3 Ultrasonic measurements

1.3.1 Velocity estimation

The ultrasonic pulse transmission technique was employed in velocity estimation using 1 MHz contact transducer with a 50 MHz digital oscilloscope. The accuracy of picking travel time in this system is 20ns and the accuracy of measuring travel distance (by a digital caliper) is 0.01mm, which amounts to a total error bar of 0.2% for estimating compressional wave velocity and 0.25% for shear wave velocities. The acquisition type used was transmission. One transducer as the source and another as receiver. Travel times were then picked directly from the digital oscilloscope and velocity values were inverted. Acquisition parameters listed in Table 1.

Table 1.1: Acquisition parameters and estimated velocity in blocks C1 and C4.

Frequency of Transducer	1MHz
Glass Velocity	5800m/s
Dominant Wavelength	5.8mm

The transmission experiment was carried out in different directions on the glass blocks. On Model C1, velocities were observed to be slowest when propagating perpendicular vertically aligned fractures. Figure 1.14 shows results of compressional wave velocity measurements on Model C1; colored ribbons

represent the positions of transmitting and receiving transducers. Maximum compressional wave velocity of 5810 m/s is observed in a travel path with no embedded fractures. Transmission along the fracture plane also displays similar velocities (5805 m/s). However, transmission perpendicular to vertical fractures showed delay of about 1% (5780 m/s). This result, although not surprising shows that compressional wave velocities reduce on encountering fractures.

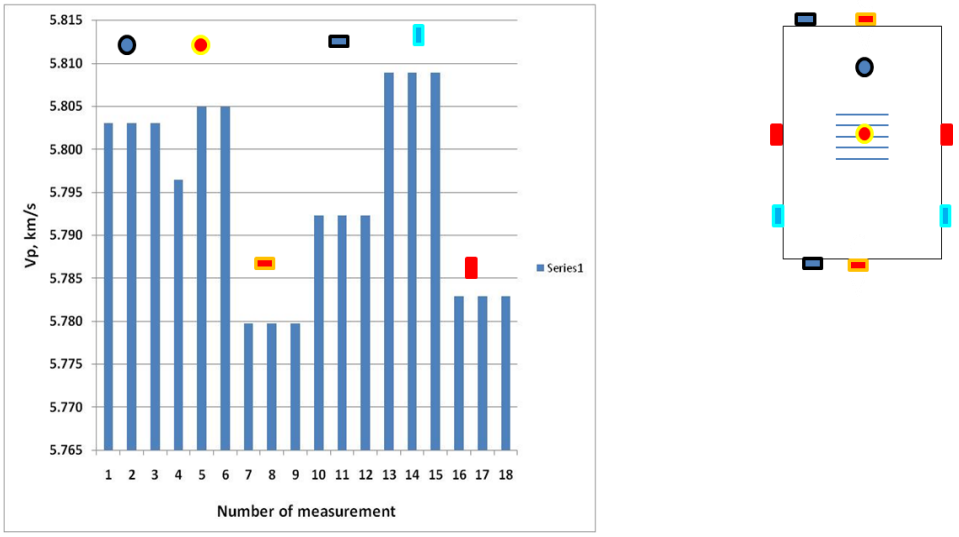

Figure 1.14. Results of compressional wave velocity measurements on Model C1; ribbons represent positions of source and receiver transducers.

Similar experiments were repeated for C4 and compressional and shear wave velocity measurements were taken in different directions as well. Results are displayed in Figure 1.15. Note that C4 is the model with a mistaken fracture. This fracture has a larger lateral extent as compared to other fracture sets and is probably filled with melted glass. This could be likened to a vertical fracture set

in a geologic setting filled with low density materials. These materials ultimately reduce the stiffness coefficients of the rock. Once again, maximum P-wave velocity is through plain glass (5810 m/s); velocities are also similar when propagation is along vertical fractures. However, the velocity of P-wave propagating perpendicular to vertical fractures is much lower in C4 than in C1. There is a 2.5% drop in velocity when propagating across fractures in C4 compared to C1. This translates to an anisotropic epsilon ε of 0.025.

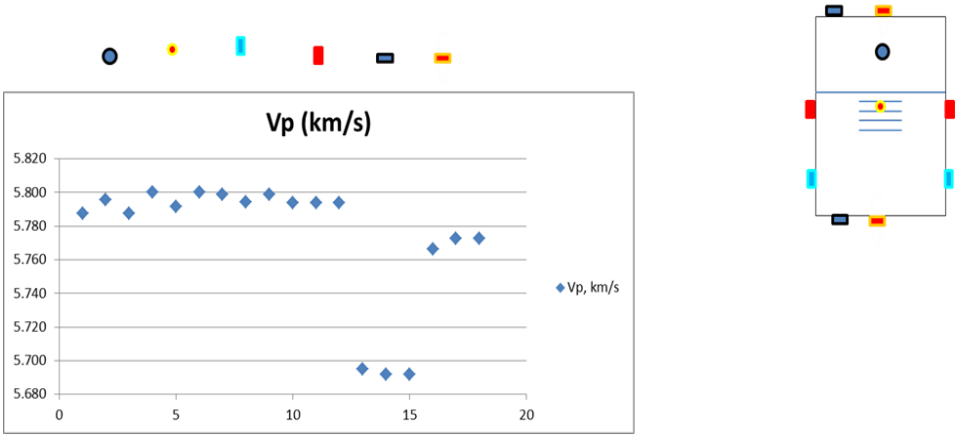

Figure 1.15. Results of compressional wave velocity measurements on Model C4; ribbons represent positions of source and receiver transducers.

Shear wave velocity measurements on Model C4 also displayed similar results, and they are displayed in Figure 1.16. Shear waves show far higher sensitivity to these fractures. Maximum delay is about 5%.

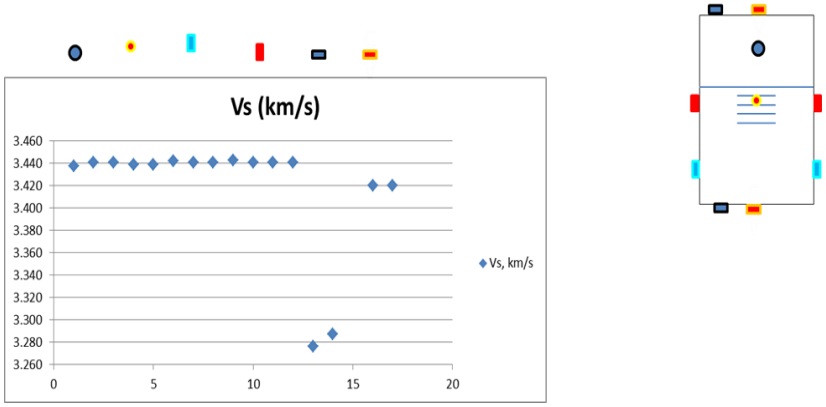

Figure 1.16. Results of shear wave velocity measurements on Model C4; ribbons represent positions of source and receiver transducers.

1.3.2 Amplitude measurements

Peak amplitude values were picked directly from oscilloscope display and plotted against direction of compressional wave propagation. Results are displayed in Figure 1.17.

These results were analyzed in pairs because of attenuation. As the composite model was not a cube, the propagation distances could be very dissimilar. In all pairs of measurements, we can observe that higher peak amplitude occurs when travelling through a fracture zone. This may be due to increased scattering or to an increased coda signature.

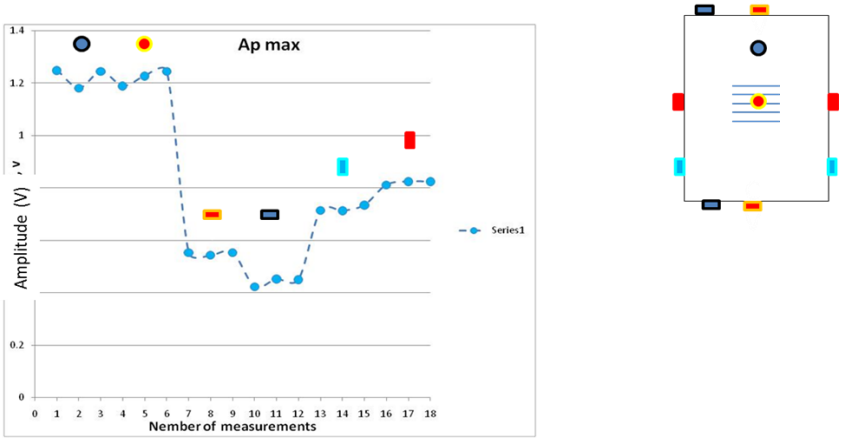

Figure 1.17. Compressional wave peak amplitude measurements on Model C1; ribbons represent positions of source and receiver transducers.

1.4 3D transmission measurements

A seismic transmission survey was run over Models C3 and C4 side by side with 10cm separation. The transmission experiment was carried out in AGL's marine measurement system (acoustic tank) with 300 KHz spherical transducers. It was a common offset experiment with source and receiver distance from the block at 0.5cm. All other parameters are listed in Table 1.2. There was also a 0.25cm receiver separation which meant there were 4 traces per cm.

Table 1.2. Acquisition parameters for ultrasonic transmission experiment on Models C3 and C4.

Acquisition Type	Common Offset SST
Minimum/Constant Offset	2cm
Number of Lines (InLines)	60
Number of Source Points (CrossLines)	100
Receiver/Shot Interval	0.25cm
Vertical Stack Fold	20
Total Number of Traces	40,000

The experiment was carried out in the marine acquisition system of the AGL. The tank was filled with water and submersible spherical transducers were used. The experiment was a physical modeling experiment with a scaling factor of 1:10,000. In practice, wavelength, frequency and sample rate are scaled on the order of 10,000 to match a real world scenario; for example, a physical modeling measurement of 300 KHz frequency and 0.2μs sample rate will be scaled to 30 Hz, with a sample rate of 2ms. Velocity of seismic wave in this medium remains the same and it is assumed that other physical phenomena, such as attenuation, Q, shear wave velocity and density remain unchanged. In the case of this experiment, the acquisition is an assemblage of 2D common offset transmission experiments to make a 3D volume. Figure 1.18 is a schematic of the transmission experiment.

Figure 1.18. Schematic of transmission experiment on C4 and C3.

Figure 1.19 is the resulting mid-inline transmission section. Notice diffraction due to the large crack on Model C4. The transmission section was also plotted into a 3D modeling software.

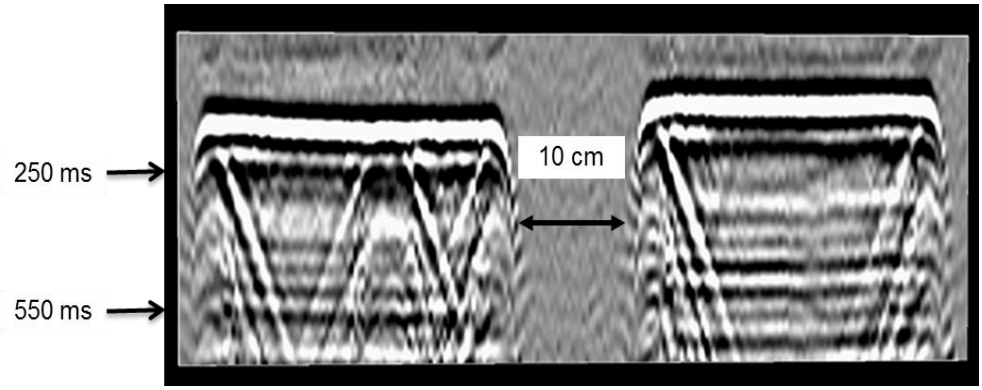

Figure 1.19. Seismic section resulting from transmission experiment (time scaled by a factor of 10,000).

Figure 1.20 is a time slice through the transmission volume. Notice the high amplitude onset of embedded fractures on Model C4. This is in agreement with the ultrasonic measurements presented in Section 1.3.

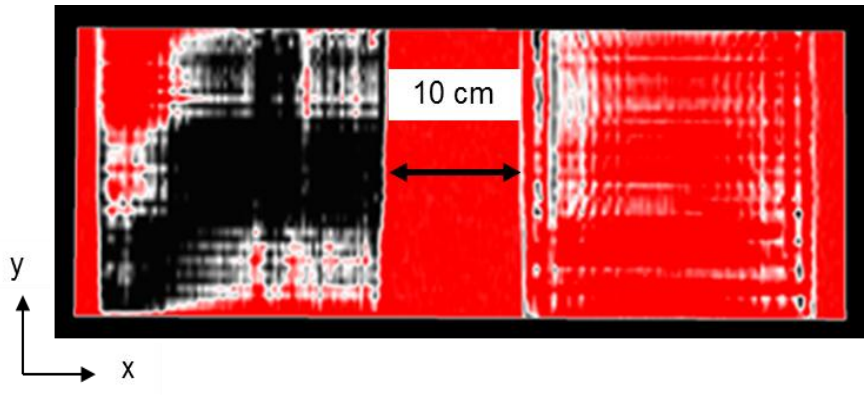

Figure 1.20. Time slice through transmission seismic volume at 350ms.

1.5 Surface seismic non-hyperbolic moveout measurements

In this section, we present surface seismic experiments that were carried out on three glass models, namely C3, C9 and C10. Once again, C3 served as the calibration model; Models C9 and C10 were designed to simulate combinations of VTI and HTI symmetries. C9 had a combination of HTI and VTI symmetries and C10 was a VTI model (shown in Figure l.13). In both C9 and C10, horizontal fractures were separated by 0.3 cm and 0.5cm at the top and bottom. Vertical fractures in C9 had an aperture of 0.5cm. The major aim of this new set of experiments was to better understand the relationship between fracture orientation and seismic non-hyperbolic moveout. The acquisition parameters for all experiments performed on the three models are listed in Table 1.3

Table 1.3. Acquisition parameters for seismic non-hyperbolic moveout test on Models C3, C9, and C10 (scaling factor 1:10000).

Minimum Offset	400m
Maximum Offset	2000m
CMP Interval	20m
Depth of Model	800m (TWT to end of model = 350ms)
Average Velocity of Model	5800m/s
Dominant Frequency/ Wavelength	120 Hz / 50m

This was a physical modeling experiment with a scaling factor of 1:10,000, so all offset, time and frequency measurements in Table 1.3 were scaled by a factor of 10,000. In order to observe residual eta $\boldsymbol{\eta}$ in a VTI formation, offset must be much greater than the depth of investigation (*i.e.*, X/D >> 1), Alkhalifah, (1997). In all experiments, maximum offset is 2000m.

These experiments were intended to test specific field problems being encountered in the Bakken Formation shale play. In the Bakken Formation, a productive clastic dolomite sequence called the middle member is sandwiched between two shale members (called the upper and lower members). This middle member is believed to be more productive when open vertical fractures exist. The existence of these open vertical fractures is believed to give the dolomite sequence a net HTI symmetry, while the upper and lower shale members will have VTI symmetry due to the presence of shales. Model C9 was designed specifically to mimic this sequence. This set of experiments hoped to uncover the

relationship between the orientation of fractures in the Bakken Formation and measured seismic velocities. Chapters 3 and 4 are dedicated to problems and solutions relating to filed studies of the Bakken Formation.

1.5.1 Acquisition - Model C3

Figure 1.21 is a schematic of the control experiment conducted on Model C3. Figure 1.22 is the resulting raw CMP gather.

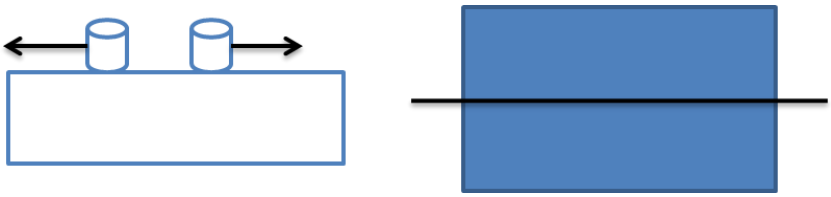

Figure 1.21. Schematic of surface experiment on Model C3. a) side view of Model C3 with transducers moving away from each other for a CMP acquisition; b) aerial view of experiment with black line representing acquisition line.

Notice events corresponding to surface wave arrivals and reflections from the bottom of the model. There is no reflection from inside the block itself because it is a blank glass sample. Although not surprising, it is a good QC to see no internal reflection from the calibration model. This way, we can attribute all events between 0 and 350 ms to reflection or diffraction from fractures.

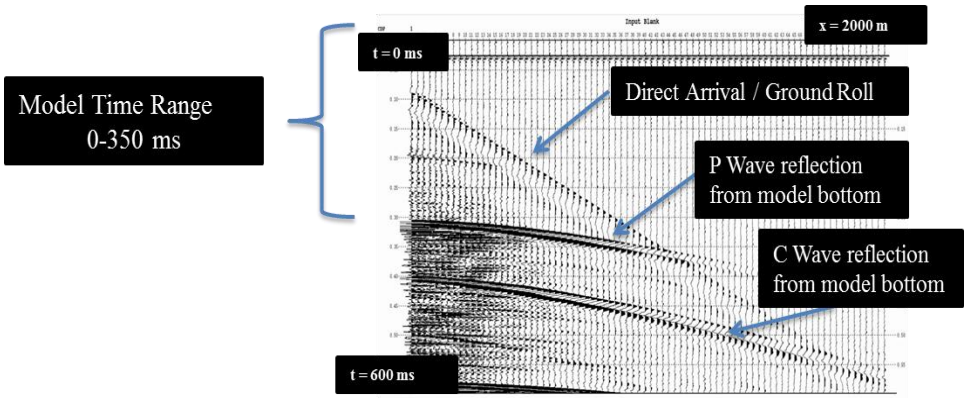

Figure 1.22. Raw CMP gather from surface experiment on Model C3; notice surface and body wave arrivals.

Another way to distinguish among, events in this kind of scenario is by velocity analysis. Since compressional and shear wave velocities of glass is known, we can attribute velocity semblance plots to types of events. This understanding also prepared the data for residual curvature tests. Figure 1.23 shows velocity analysis of the data from Figure 1.22. Most events have velocities closer to their corresponding ultrasonic velocities. This further confirms the identity of these individual events. It also supplies us with a velocity profile for NMO correction.

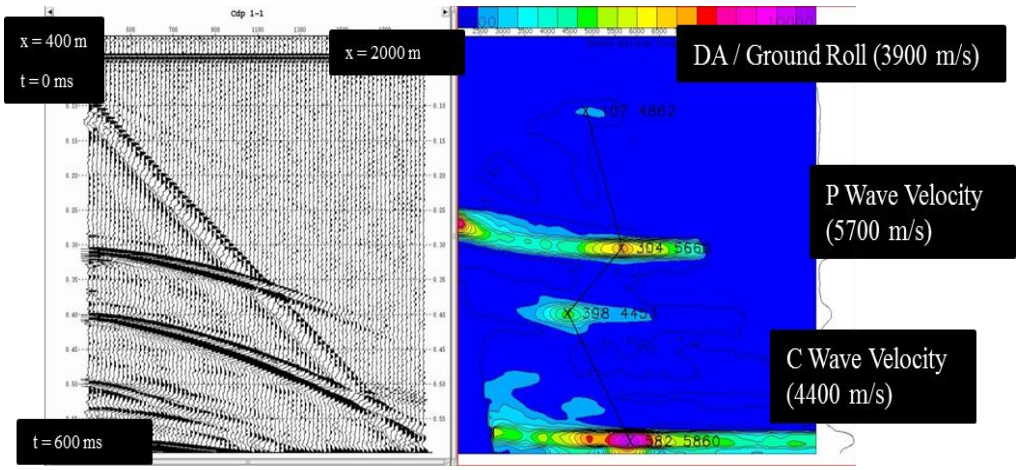

Figure 1.23. Stacking velocity analysis semblance plot on raw CMP gathers from Model C3.

1.5.2 Acquisition - Models C10 and C9

Similar experiments to Model C3 were conducted on C4, (these were shown in Table 1.3). This time around, reflections were expected before 350 ms. Figure 1.24 shows a schematic of the experiment.

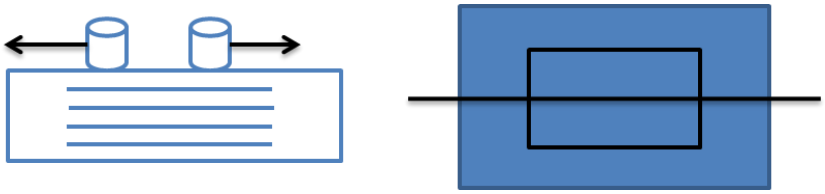

Figure 1.24. Schematic of surface experiment on Model C10. a) side view of Model C10 with transducers moving away from each other for a CMP acquisition; b) aerial view of experiment with black line representing acquisition line and black inner box showing region of horizontal fractures.

To determine the effect of fracture orientation on seismic velocities, three seismic lines were acquired on Model C9. The lines were labeled Azimuth 0, Azimuth 45, and Azimuth 90. The zero azimuth line is the CMP line acquired in-line with the middle vertical fractures and Azimuth 90 is perpendicular to those fractures. Azimuth 45 is in between both Azimuths 0 and 90.

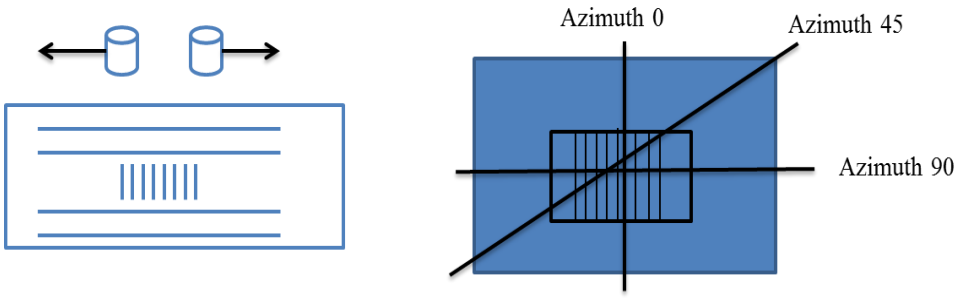

Figure 1.25. Schematic of surface experiment on Model C9. a) side view of Model C10 with transducers moving away from each other for a CMP acquisition; b) aerial view of experiment with black line representing acquisition line and black inner box and lines showing region of embedded horizontal fractures and sandwiched vertical fractures.

1.5.3 Processing

The processing technique of choice for this physical modeling data is parabolic radon transform. This is to make sure reflection events were continuous and attenuate irregular events. Results of radon transform on Model C3 are shown in Figure 1.26. Once again, no noticeable reflections appeared before 350 ms. Radon transform seems to have attenuated all linear events in the data (ground roll and direct arrivals).

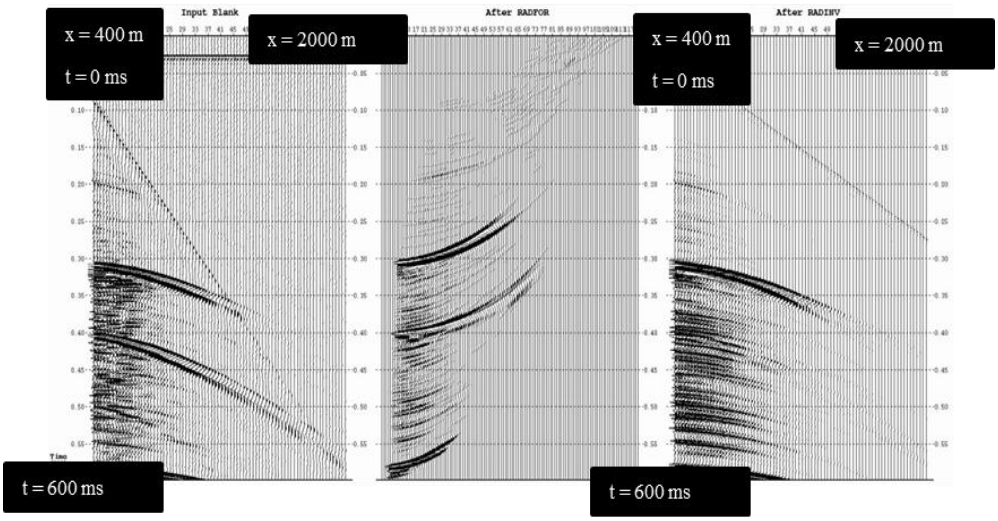

Figure 1.26. Parabolic Radon transform noise attenuation technique applied to Model C3. a) Raw CMP gather; b) after forward Radon transform (τ – p domain); c) after inverse Radon transform.

Similar noise attenuation technique was applied to Models C9 and C10. From Figure 1.27, we can clearly see radon transform attenuating linear events and enhancing parabolic (reflection) events.

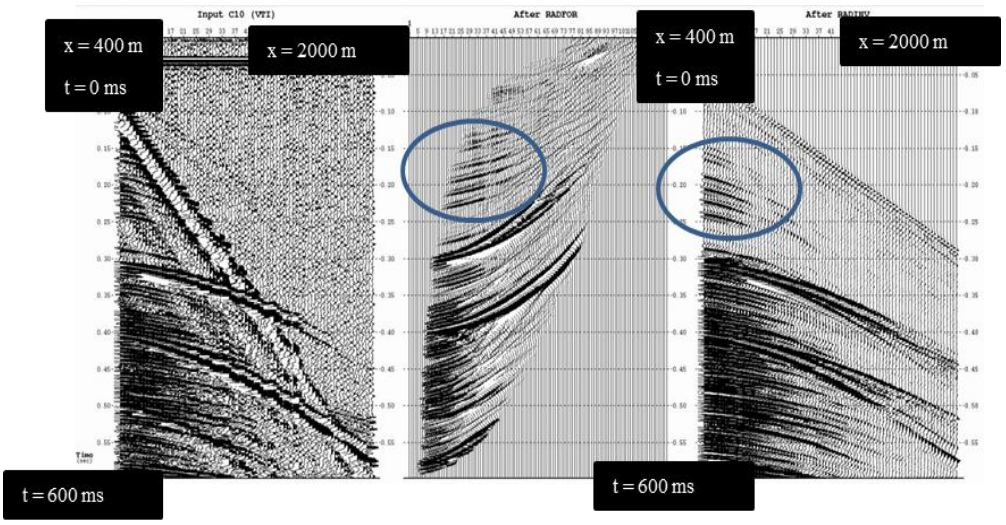

Figure 1.27. Parabolic Radon transform noise attenuation technique applied to Model C10. a) Raw CMP gather; b) after forward radon transform (τ – p domain); c) after inverse radon transform (Area in blue circle represents reflection from horizontal layers in Model C10).

.

1.5.4 Residual eta ($\boldsymbol{\eta}$) measurements

There are five set of CMP data to be analyzed: one each from Models C3 and C10 and three from Model C9; the latter represents three different source receiver azimuths.

After analyzing stacking velocity semblance plots and picking velocities, we plotted residual eta semblance plots and observed residual curvature on NMO corrected CMP gathers. Residual eta semblance plots for Models C3 and C10 are displayed in Figure 1.28; the maximum $\boldsymbol{\eta}$ for the blank glass model (C3) is zero.

This further confirms the absence of reflection events in the model and hence makes a stronger argument to make it a calibration model.

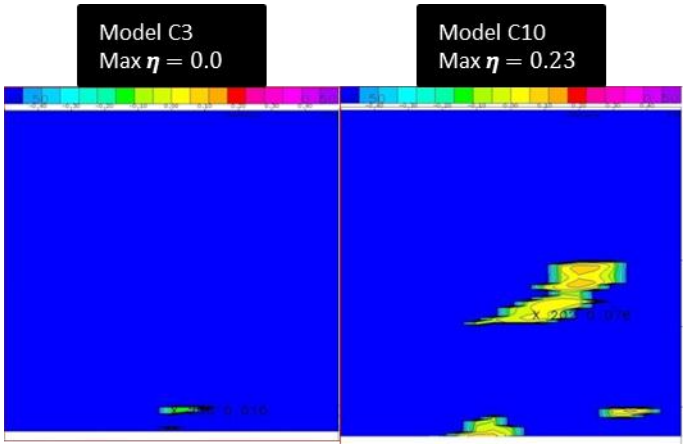

Figure 1.28. Residual eta semblance plots for models C3 and C10 showing maximum residual eta values.

In Figure 1.29, all residual eta semblance plots for three different source receiver azimuths on Model C9 are displayed.

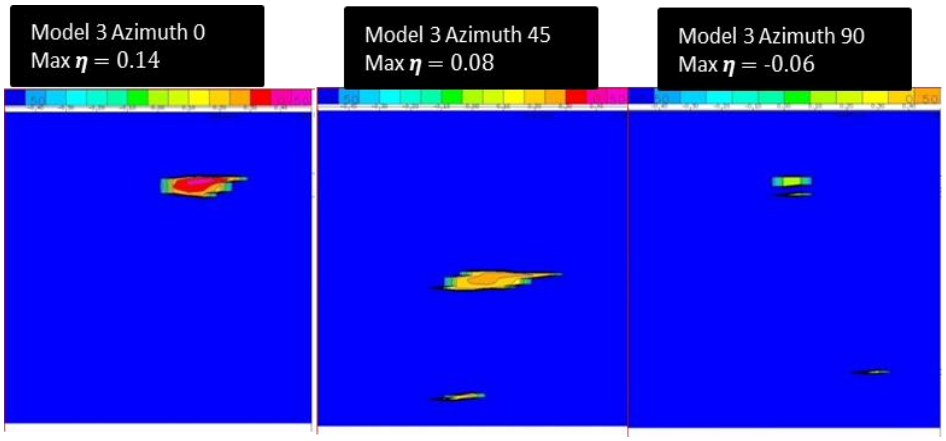

Fig 1.29. Residual eta semblance plots for Models C9. a) Azimuth 0; b) Azimuth 45; c) Azimuth 90. Maximum $\boldsymbol{\eta}$ values also displayed.

Table 1.4 lists the five acquisition types attempted in this project against corresponding maximum residual $\boldsymbol{\eta}$.

Table 1.4. Model and acquisition type against maximum residual $\boldsymbol{\eta}$

Model Description	Maximum residual $\boldsymbol{\eta}$
C3 Single Azimuth	0.00
C10 Single Azimuth	0.23
C9 Azimuth 0	0.14
C9 Azimuth 45	0.08
C9 Azimuth 90	-0.06

The maximum $\boldsymbol{\eta}$ value is recorded in Model C10 (the VTI model) and the minimum is recorded in C9 Azimuth 90 (or C3 the blank model). These results show that the more VTI-like a medium is the higher or more reliable the residual $\boldsymbol{\eta}$ will be. Within the limit of this experiment, we found the highest $\boldsymbol{\eta}$ values were from C10 (the purely VTI model) and C9 Azimuth 0.

In Model C9 Azimuth 0, the direction of the propagation of seismic waves is in line with the vertical fracture set and so is mildly affected by these fractures. This scenario (C9 Azimuth 0) can be likened to a VTI case as the effect of the vertical fractures is minimal. However, the lowest $\boldsymbol{\eta}$ values were recorded for seismic waves travelling perpendicular to the vertical fractures.

Chapter 2

Experimental investigation of stress and fracture-induced seismic anisotropy

2.1 Introduction

Anisotropy in the Earth can be caused by aligned heterogeneities. These heterogeneities are in different forms and scales. Anisotropy in shales is due to micro-fissile structure of clay which gives it an effective VTI symmetry. HTI anisotropy, on the other hand, is due to vertically aligned heterogeneities in the of form fractures due to regional stress. These types of heterogeneities sometimes combine to form orthorhombic or monoclinic symmetry. In the case of shale oil or gas, most hydrocarbons reside in open vertical fractures (Pitman et al. 2001). As a result, orthorhombic symmetry may be a realistic anisotropic model for these systems.

To study the effect of stress in a layered orthorhombic medium (as in the case of shale oil and gas), a physical modeling study using intrinsically orthorhombic phenolic boards was conducted. The experiment was designed to simulate

sedimentary reservoir rocks deposited in layers with inherent orthotropic symmetry and under the influence of stress due to overlying sediments. The study presented in this chapter explored which geologic phenomena dominate the contortion of anisotropy under different stress tenures. Phenolic boards were coupled together with the help of a pressure device and uniaxial stress was gradually increased while time arrival and velocity measurements were repeated. A combination of parallel vertical fractures due to regional stress and a background horizontal layering combine to form orthorhombic symmetry. Due to fact that these two geologic phenomena (horizontal layering/stratification and regional stress) are widespread, orthorhombic symmetry may be a truly realistic anisotropic earth model for reservoir characterization. We considered the effect of simulated overburden pressure on phase velocity, stiffness coefficients and anisotropic parameters in a layered orthorhombic medium. The layered medium consists of 55 1.5mm-thick phenolic slabs or boards coupled together with a pressure apparatus. Figure 2.1 is a snapshot of the composite model showing all dimensions and principal directions. Phenolic CE is an industrial laminate with intrinsic orthorhombic symmetry.

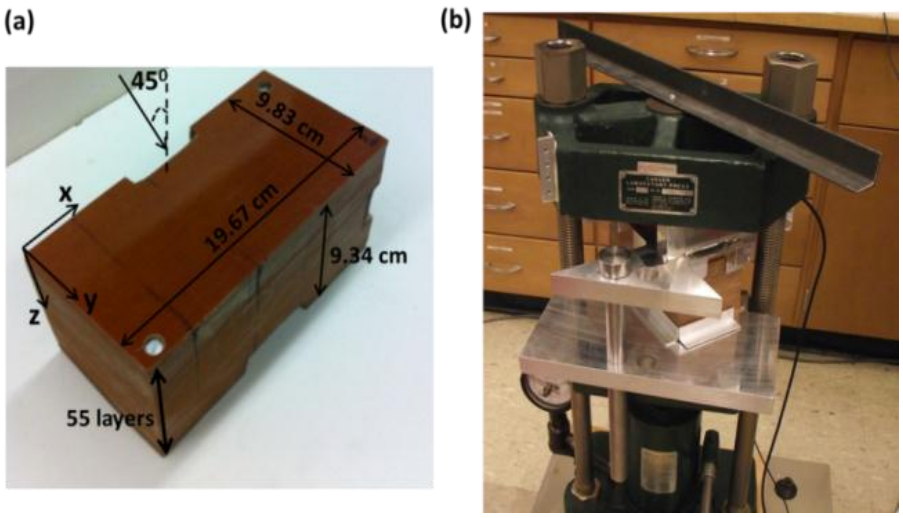

Figure 2.1. Snapshots of physical model and experimental setup. (a) Phenolic model showing all principal directions; (b) AGL designed pressure apparatus with phenolic model embedded.

Scaled ultrasonic seismic measurements were taken in radial, sagittal, and traverse directions on all block faces, and travel times were picked directly from a digital oscilloscope and inverted for compressional and shear wave velocities as well as anisotropic parameters. Uniaxial stress was gradually increased and all measurements were repeated.

The experiment was designed to simulate earth-like intrinsically anisotropic rocks which are buried in layers and thus under the influence of pressure from overburden sediments. Previous measurements by Pervukhina and Dewhurst (2008) showed the relationship between anisotropic parameters and mean effective stress in transversely isotropic shale core samples. In this experiment, we

extended a similar approach to a physical model of orthotropic symmetry. In a seismic physical modeling experiment, an attempt is made at estimating the seismic response of a geologic model by measuring the reflected or transmitted wave field over the scaled model (Ebrom and McDonald, 1994). The scaling is on travel time and consequently wavelength but all other wave attributes, such as velocity, remain intact. In physical modeling, it is assumed with a fair degree of accuracy that the physics of elastic wave propagation in the physical model is the same as that in the real world. This could be explained by infinitesimal strain elastic wave theory (Ebrom and McDonald, 1994). The main objectives of the experiment presented in this chapter are as follows:

1) To explore the effect of stress on anisotropy in an inherently anisotropic medium.

2) To explore which physical phenomena (horizontal layering/stratification or vertical fractures) dominate the character of anisotropy as uniaxial stress increases. Our results show anisotropic behavior ascribable to both orthorhombic symmetry and VTI symmetry due to layering. Anisotropic behavior attributable to polar anisotropy tends to increase with increasing uniaxial stress.

2.2 Experimental setup

Fifty-five phenolic boards were bound together by an AGL-fabricated pressure device connected to pressure and strain gauges. Figure 2.2 is a schematic of the experimental setup. The principal axes of the composite model are labelled X, Y, and Z, with Z being the direction perpendicular to layering (or sedimentation/stratification in a real earth case). The Z direction is also the direction of much interest to exploration geophysics. Following other orthorhombic anisotropy publications, X=1, Y=2, and Z=3. The thickness of the phenolic boards ranged from 1.4 mm to 1.7 mm. Before the commencement of travel time measurements, density measurements were taken and a strain test was conducted mainly to test the elastic strength of the composite model.

Figure 2.3 shows a stress-strain curve for the model. Uniaxial stress was increased from 0.05MPa to 0.5MPa; in all, 7 sets of measurements were taken. 100 kHz compressional and shear transducers were used to ensure seismic wavelength was at least 10 times the thickness of each phenolic sheet. The wavelength of the compressional wave was measured at ~30 mm (thickness of phenolic board ~1.5 mm). In all measurements (both compressional and shear wave), $\lambda \gg H$ (λ is seismic wavelength and H is the thickness of the phenolic board). This was to ensure an effective seismic response from the whole model rather than scattering between layers.

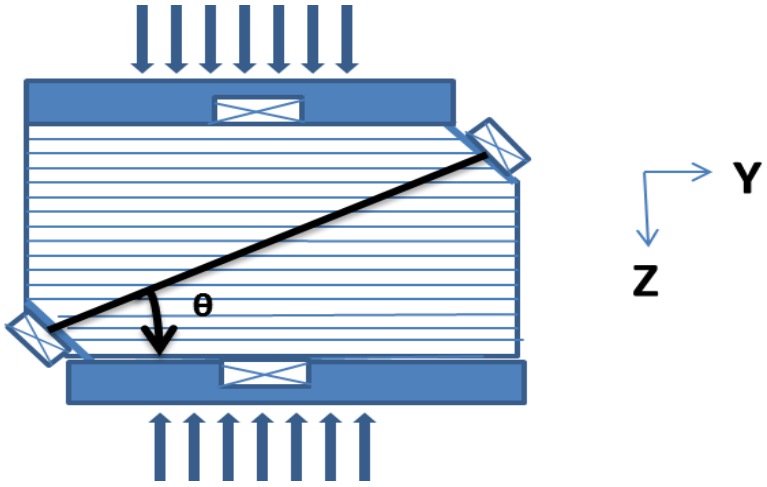

Figure 2.2. Schematic of experimental setup showing direction of the application of stress and position of ultrasonic transducers. **θ** is the phase (wavefront) angle and it differs in different axes because the composite model is a cuboid (45^0 in ZY, 25.4^0 in ZX and 26.6^0 in XY).

The source and receiver transducers were placed on opposing sides for a pulse transmission measurement. The polarization direction of the shear transducer varied from 0^0 to 180^0 and measurements were taken at 10^0 interval. In each case, 0^0 was shear polarization parallel to the bedding plane and 90^0 was polarization perpendicular to the bedding plane. Compressional and shear wave arrivals were picked directly from seismograms produced by the AGL-scaled ultrasonic system, with an accuracy of ± 0.1μs. In this experiment, travel time measurements were inverted for phase velocities; this is because the transducers were relatively wide compared to the thickness of the model being measured (Dellinger and Vernik, 1994) . The diameter of the transducers used (both compressional and shear) was

4cm. Transducer response had been studied for directivity and delay time. Time arrival measurements were taken at 3 principal axes, Z (3), X (1), and Y (2). Diagonal phase velocity measurements were also taken at 45^0 on the ZY axes and at two other oblique angles: 25.4^0 at ZX and 26.6^0 at XY; this was due to the fact that the composite model is a cuboid (as was shown in Figure 2.1a). The dimensions of the model were 19.67 cm X 9.83 cm X 9.34 cm. As a result, angle dependent velocities were used across the ZX and XY axes to obtain diagonal stiffness coefficients ($C_{12}\ and\ C_{23}$). The signal scaling factor was 1:10000. All model construction as well as ultrasonic measurements were carried out at the AGL at the University of Houston.

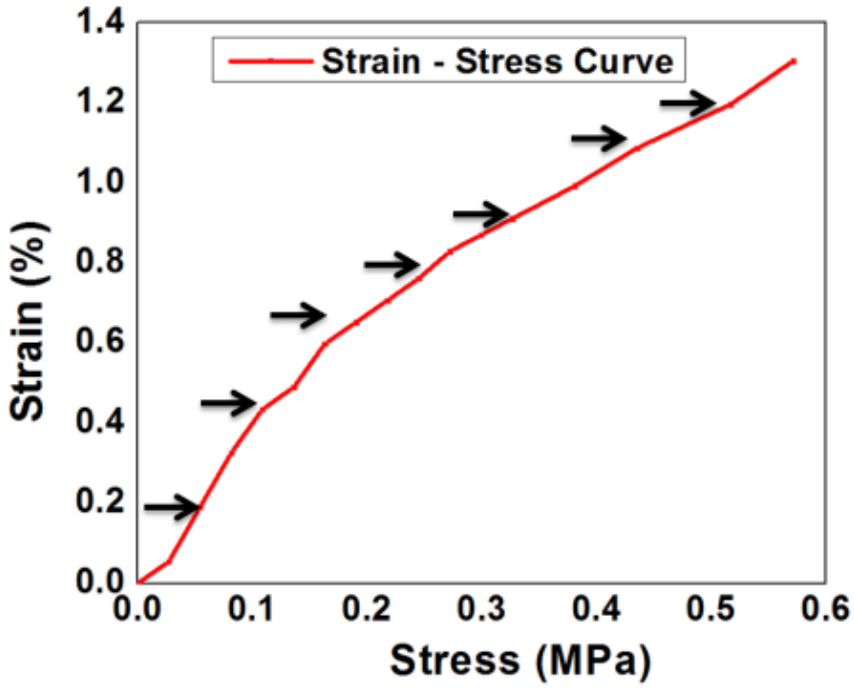

Figure 2.3. Stress-strain curve for layered phenolic. Black arrows indicate chosen values for velocity and anisotropy measurements.

2.3 Phase velocity measurements

Figure 2.4 shows compressional wave velocities as a function of uniaxial stress (overburden pressure) in all measured directions. Not surprisingly, P-wave velocity increased with pressure in all directions. This is due to a gradual closure of space between layers in the model. P-wave velocity in the Z direction is significantly lower than in the X and Y directions due to laminate finishing of the phenolic model used. Diagonal P-Wave measurements also show an overall increase with stress. Figure 2.4a shows phase velocities in ZX (25.4^0), ZY (45^0)

and XY (26.6^0) as they vary with stress.

Shear wave splitting was observed and recorded in all principal directions during the course of the experiment. Fast and slow shear wave arrivals were observed and inverted for both stiffness coefficients and anisotropic parameters. Figure 2.5 displays a scaled shear wave seismogram as a function of polarization angle (0^0 to 180^0 every 10^0) in 3 different stress systems (0.16MPa, 0.33MPa and 0.52MPa). Signal scaling factor is 1:10000. Notice the decrease in arrival time for both fast (S1) and slow (S2) shear waves as stress increases. Figure 2.6 is a plot of fast and slow shear wave velocities as uniaxial stress increases.

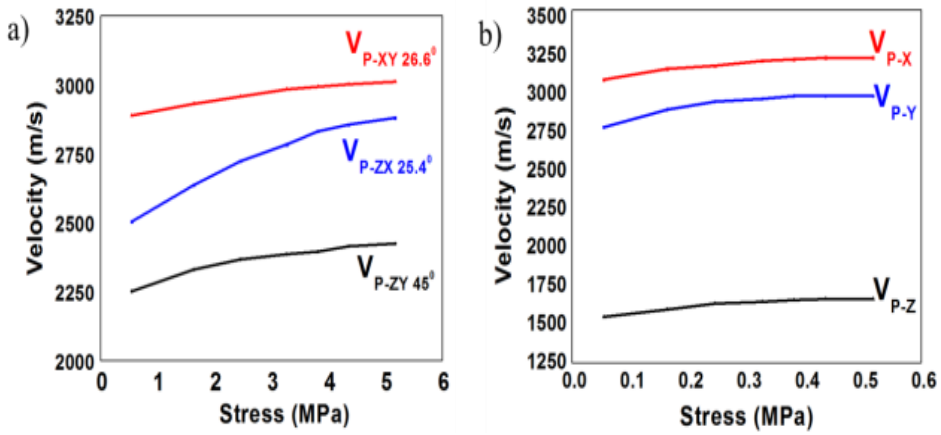

Figure 2.4. Compressional wave velocities as function of uniaxial stress in all measured directions (P-wave velocity uncertainty is ± 0.15%).

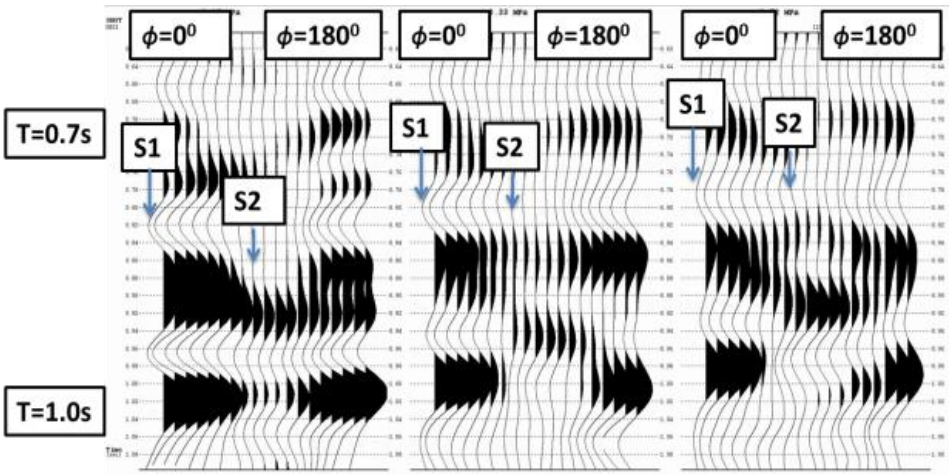

Figure 2.5. Shear wave seismogram, as a function of shear wave polarization ($\boldsymbol{\phi}$) in different stress regimes (0.16MPa, 0.33MPa and 0.52MPa).

It can be observed from Figure 2.6 that velocities of fast and slow shear waves largely increased with uniaxial stress. Also, the delay between fast and slow shear waves tended to generally diminish in all planes of measurement. However, in the Z direction, delay between fast and slow shear waves approached a minimum; this is diagnostic of polar anisotropy (VTI). In a polar anisotropy symmetry (specifically VTI), $V_{s1(Z)} = V_{s2(Z)}$ because only one axis of symmetry exists.

2.4 Stiffness coefficients

Elastic constants were derived from density and velocity measurements. P-wave dependent stiffness coefficients were computed using the following equations,

$$C_{11} = \rho Vp(x)^2 \quad (2.1a)$$

$$C_{22} = \rho Vp(y)^2 \quad (2.1b)$$

$$C_{33} = \rho Vp(z)^2 \quad (2.1c)$$

Shear wave dependent elastic constants were calculated using the Tsvankin (1997) extension of Thomsen's (1986) equation for orthorhombic models. In this case, it manifests as an averaging of fast and slow shear wave velocities across adjacent axes according to the following equations:

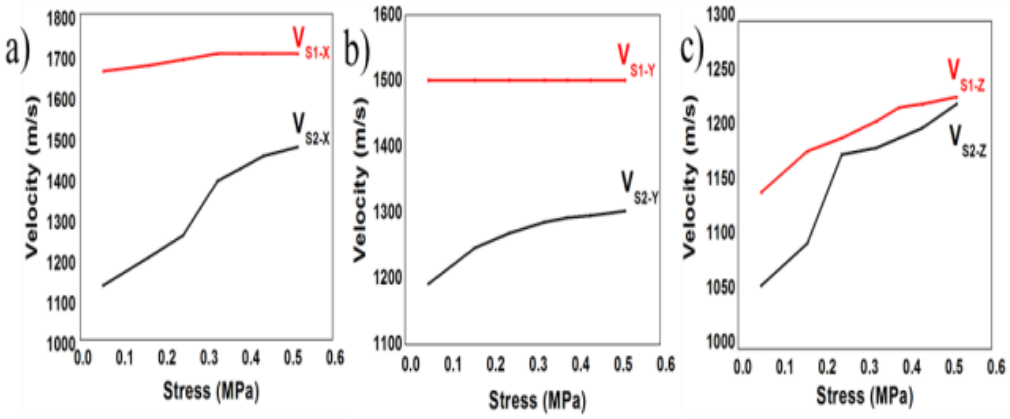

Figure 2.6: Fast and slow shear wave velocities in X (1), Y (2), and Z (3) directions as a function of uniaxial stress (S-wave velocity uncertainty is ± 0.3%).

$$C_{44} = \rho \left(\frac{V_{s2(y)} + V_{s2(z)}}{2} \right)^2 \quad (2.2a)$$

$$C_{55} = \rho \left(\frac{V_{s1(z)} + V_{s2(x)}}{2} \right)^2 \quad (2.2b)$$

$$C_{66} = \rho \left(\frac{V_{s1(y)} + V_{s2(x)}}{2} \right)^2 \quad (2.2c)$$

Diagonal stiffness coefficients, however, were computed using a polar anisotropy assumption in each block face (or principal axis). Unambiguously a VTI assumption was used in ZX and ZY axes and HTI in XY plane. Bearing in mind that we did not have exact 45^0 angles in some diagonal measurements, we have

used an angle dependent form of Thomsen's (1986) equation and this eventually collapses to the more common diagonal elastic constant equations at 45^0 angles:

$$C_{13} = \left[\frac{A_{13}-B_{13}}{4\sin^2\theta\cos^2\theta}\right]^{0.5} - C_{44} \quad (2.3)$$

where

$$A_{13} = [2\rho Vp_{zx}^2 - (C_{11} + C_{44})\sin^2\theta - (C_{33} + C_{44})\cos^2\theta\,]^2 \quad (2.3a)$$

$$B_{13} = [(C_{11} - C_{44})\sin^2\theta - (C_{33} - C_{44})\cos^2\theta\,]^2 \quad (2.3b)$$

Also, $$C_{12} = \left[\frac{A_{12}-B_{12}}{4\sin^2\theta\cos^2\theta}\right]^{0.5} - C_{66} \quad (2.4)$$

where

$$A_{12} = \left[2\rho Vp_{xy}^2 - (C_{11} + C_{66})\sin^2\theta - (C_{22} + C_{66})\cos^2\theta\,\right]^2 \quad (2.4a)$$

$$B_{12} = [(C_{11} - C_{66})\sin^2\theta - (C_{22} - C_{66})\cos^2\theta\,]^2 \quad (2.4b)$$

And, $C_{23} = \left[\frac{A_{23}-B_{23}}{4\sin^2\theta\cos^2\theta}\right]^{0.5} - C_{55}$ (2.5)

where

$$A_{23} = \left[2\rho V p_{zy}^2 - (C_{22} + C_{55})\sin^2\theta - (C_{22} + C_{55})\cos^2\theta\right]^2 \quad (2.5a)$$

$$B_{23} = [(C_{22} - C_{55})\sin^2\theta - (C_{22} - C_{55})\cos^2\theta]^2 \quad (2.5b)$$

This equation generally decomposes to the following when $\theta = 45^0$,

$$C_{13} = \left[\frac{\left(4Vp45(zx)^2 - C_{11}-C_{33}-2C_{44}\right)^2 - (C_{11}-C_{33})^2}{4}\right]^{0.5} - C_{44} \quad (2.6)$$

Similar assumptions were used to calculate C_{23} *and* C_{12} (HTI approximation was used for C_{12}), for example:

$$C_{12} = \left[\frac{\left(4Vp45(xy)^2 - C_{11}-C_{22}-2C_{66}\right)^2 - (C_{11}-C_{22})^2}{4}\right]^{0.5} - C_{66} \quad (2.7)$$

$$C_{23} = \left[\frac{\left(4Vp45(zy)^2 - C_{22} - C_{33} - 2C_{55}\right)^2 - (C_{22} - C_{33})^2}{4}\right]^{0.5} - C_{55} \quad (2.8)$$

Figure 2.7 shows compressional and shear wave dependent as well as diagonal stiffness coefficients as functions of uniaxial stress. Once again, C_{33} is low (Figure 2.7a) in comparison to the rest due to the nature of the phenolic material being used.

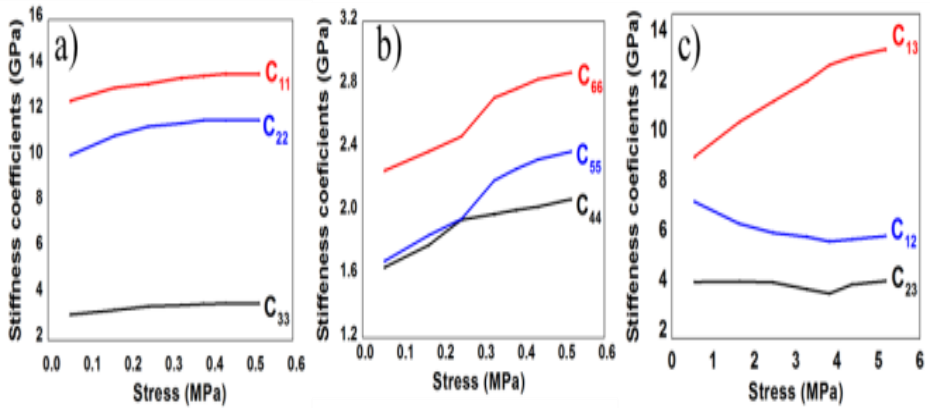

Figure 2.7: Stiffness coefficients as a function of uniaxial stress

Generally, within the limit of this experiment, all stiffness coefficients tended to increase with uniaxial stress (except C_{12} *and* C_{23} which tended to remain constant). Diagonal elastic constants (specifically C_{12} *and* C_{23}) remain largely constant with changing stress, but C_{13} increased significantly with stress. This

may have been due to an unknown preferred orientation within the wave fabric of the phenolic model.

2.5 Anisotropic parameters

In order to quantify the anisotropy in our measurements, anisotropic parameters γ *and* ε were computed using the same extension of Thomsen's (1986) parameters (Tsvankin, 1997). Equations for compressional wave anisotropies are listed as follows:

$$\varepsilon_{xz} = \frac{1}{2}\left(\frac{V_{px}-V_{pz}}{V_{pz}}\right) = \varepsilon^2 \tag{2.9a}$$

$$\varepsilon_{yz} = \frac{1}{2}\left(\frac{V_{py}-V_{pz}}{V_{pz}}\right) = \varepsilon^1 \tag{2.9b}$$

$$\varepsilon_{xy} = \frac{1}{2}\left(\frac{V_{py}-V_{px}}{V_{px}}\right) = \varepsilon^3 \tag{2.9c}$$

For shear wave anisotropies, the equations are as follows:

$$\gamma_x = \frac{1}{2}\left(\frac{Vs1(x)^2}{Vs2(x)^2} - 1\right) = \gamma^1 \tag{2.10a}$$

$$\gamma_y = \frac{1}{2}\left(\frac{Vs1(y)^2}{Vs2(y)^2} - 1\right) = \gamma^2 \quad (2.10b)$$

$$\gamma_z = \frac{1}{2}\left(\frac{Vs1(z)^2}{Vs2(z)^2} - 1\right) = \gamma^3 \quad (2.10c)$$

Some earlier publications on orthorhombic anisotropy expressed these equations as ε^1 and γ^1. Figure 2.8 shows compressional (ε) and shear wave (γ) anisotropies as functions of uniaxial stress. Anisotropic parameter ε (Figure 2.8a) tended to remain constant in the limit of the experiment. The reason for the difference in ε_{yx} value is once more due to the nature of the composite phenolic material in the Z (or 3) direction. There is a large difference in compressional wave velocities in the X or Y directions compared tothat of Z, which explains the large values of ε_{xz} and ε_{yz} compared to ε_{yx}. Anisotropic parameter γ (Figure 2.8b) largely diminishe with increasing stress. In the Z direction (γ_z) it tended towards zero at higher stress states. This is once again diagnostic of VTI symmetry. In a VTI polar anisotropy case, $\gamma_z = 0$.

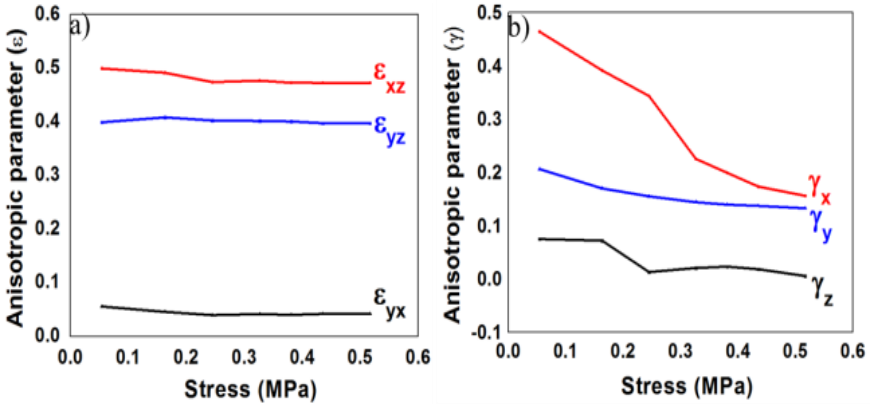

Figure 2.8. Anisotropic parameter ε (Compressional wave anisotropy) and γ (shear wave anisotropy) as a function of uniaxial stress.

2.6 Conclusion

This experimental study has investigated changes in anisotropic parameters and stiffness coefficients in an orthorhombic medium as functions of uniaxial stress. Results show maximum increase in compressional and shear wave velocities ranging from 4% to 10% in different directions as functions of increasing uniaxial stress. Compressional and shear wave dependent stiffness coefficients generally increased with stress. Anisotropic parameters (an extension of Thomsen's 1986 parameters for orthorhombic symmetry) generally diminished or remained constant with increasing pressure and changes ranged from 0% to 33%. We observed anisotropic behavior a priori to both orthorhombic and VTI symmetries in different principal axes of the model.

This experiment shows polar anisotropy (specifically VTI) symmetry appears to

dominate the character of anisotropy in the Z (or 3) direction as uniaxial stress increases. This is particularly significant because this direction represents the direction normal to stratification and the plane of most interest to exploration geophysics. However, the orthotropic nature of the composite is revealed in other directions.

Chapter 3

Survey location and geology of the Williston Basin

3.1 Introduction

The field data analyzed in this project are located in North Dakota, USA, in the Williston Basin. The data were supplied to the AGL courtesy of the Hess Corporation. Other well information was also obtained from the North Dakota Industrial Commission. The main objective was to study the anisotropic response of the productive Bakken Formation of the Williston Basin. Figure 3.1 shows a Google map view of the well and seismic survey location.

Figure 3.1. Google map of North America showing Stanley, North Dakota, the location of the Red Sky seismic survey.

3.2 Geology of the Williston Basin

The Williston Basin covers about 300,000 square miles from North Dakota and Montana in the United States to Saskatchewan and Manitoba in Canada (Figure 3.2). The Williston Basin is structurally simple and it is roughly circular with its deepest part in the center. Figure 3.3 shows a generalized stratigraphic column of the Williston Basin with gas-producing horizons in red and oil-producing formations in blue.

Figure 3.2. Map of the Williston Basin with black star showing the location Red Sky survey. (Source: http://familytreecorp.com/operations/williston-basin).

3.2.1 Pierre Formation

The Pierre Formation is a predominantly shale formation which occurs from North Dakota to New Mexico. It overlies the Niobara Formation and underlies the Fox Hill beds. It has a maximum thickness of 700 feet.

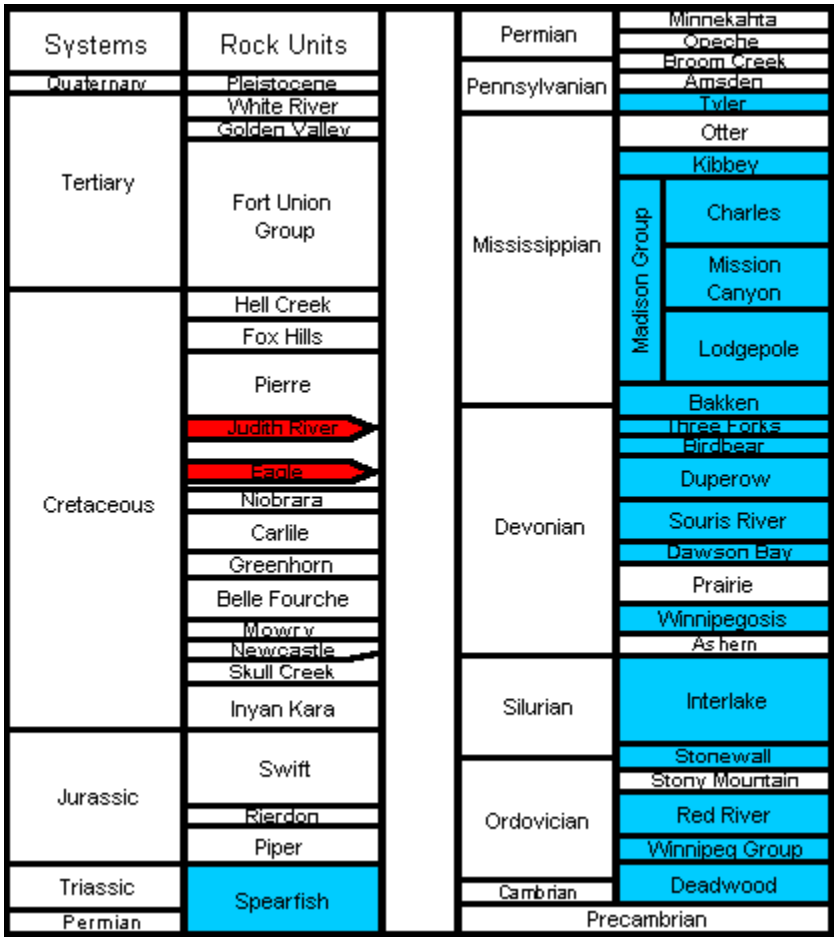

Figure 3.3. Generalized stratigraphic column of the Williston Basin with gas-producing zones in red and oil-producing zones in blue. (Source: https://www.dmr.nd.gov/ndgs/Resources/WBPetroleumnew.asp).

3.2.2 Greenhorn Formation

The Greenhorn Formation is a late Cretaceous mostly grey to black calcareous shale formation. The Greenhorn Formation has a thickness ranging from 50 to 250 feet. Greenhorn and Pierre Formations together make an approximately 1000-foot thick shale unit over the study area.

3.2.3 Bakken Formation

The Bakken Formation is a closed, low permeability petroleum system that has generated approximately 200 to 400 billion barrels of oil in place, Pitman et al, (2001). The Bakken formation overlies the Three Forks Formation and underlies the Lodgepole Formation (Figures 3.3 and 3.5). It reaches a maximum thickness of 150 feet (46 m) in the central portion of the Williston Basin and it is easily recognizable on well logs (Figure 3.4). The Bakken Formation has three distinct members: the Upper Shale Member, the Middle Clastic (productive) Member, and the Lower Shale Member. The upper and lower members exhibit very high gamma ray readings (> 200 API), high sonic slowness (80 to 120 μs/ft.), and low resistivity readings, Pitman et al, (2001). Figure 3.4 is a well log plot from 9200 to 9350 feet showing gamma ray, sonic, and shear slowness in the Bakken interval. The Middle Member exhibits typical clastic or carbonate rock characteristics. The lithology of the Middle Member is highly variable and it consists of interbedded sequences of siltstones and sandstones with lesser amounts of shale, dolostones, limestone and oolites, Pitman et al, (2001). Measured porosity in the Middle Member ranges from 1 to 16 percent, averaging about 5%. Permeability ranges from 0 to 20 millidarcies as well, averaging around 0.04 millidarcies. Core studies reveal that reservoir rocks with permeability greater than 0.01 millidarcies contain open fractures. The USGS, Pitman et al, (2001) conclude that higher permeability in the Middle Member corresponds to

open and well-developed fractures. Most oil in the Bakken petroleum system resides in open vertical fractures in the Middle Member.

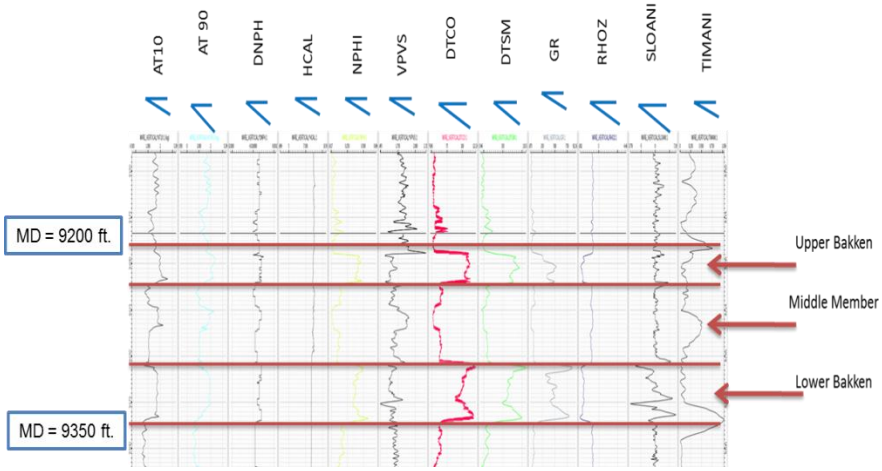

Figure 3.4. Well log from 9200 to 9350 feet. showing the three members of the Bakken Formation.

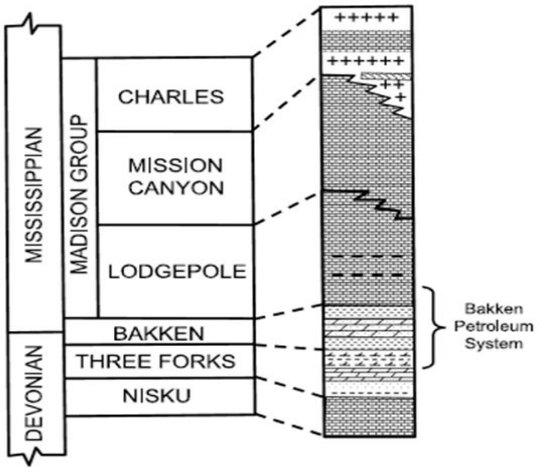

Figure 3.5. Stratigraphy of the Bakken Formation (modified from Sonnenberg and Pramudito, 2009).

3.3 Previous studies

Since the onset of oil shales at the Williston Basin, various surface seismic and micro-seismic surveys have endeavored to understand the azimuthal anisotropy and fracture distribution of the Bakken Formation. Ye et al. (2010) proposed that the different members of the Bakken Formation possess different anisotropic symmetries according to their constituent rock materials. The upper and lower shale members have intrinsic VTI symmetry while the productive middle member can be isotropic in the absence of open vertical fractures or have HTI symmetry if the fractures are present Ye et al. (2010).

Jones and Wang, (1981) took ultrasonic measurements on core samples from the Greenhorn Formation. Their intention was to understand the anisotropy of rock samples from this rock unit. As the Greenhorn is a shaley formation, they assumed polar anisotropy in their measurements. The results of their measurements are displayed in Table 3.1.

In the analysis stage of this project, Jones and Wang's (1981) stiffness coefficient values will be used to compute Thomsen's (1986) parameters and then be compared to seismic derived anisotropic parameters.

Table 3.1. Stiffness coefficients from Jones and Wang's experiment on Greenhorn shales.

Stiffness Coefficients	C_{11} (Kbar)	C_{33} (Kbar)	C_{44} (Kbar)	C_{66} (Kbar)	C_{13} (Kbar)
	343	227	54	106	107

3.4 Red Sky well survey

A total of 7 wells were analyzed during the course of this project. Well RS-NELSON_156_-91-1423H-1 is at the location at which two 2D Lines cross and it is also the well supplied directly by the Hess Corporation. All other well data was obtained from the NDIC (North Dakota Industrial Commission). Table 3.2 gives basic details of all the 7 wells used in this thesis. All wells are horizontal wells designed to snake through the productive Bakken Formation. Figure 3.6 shows a base map view of all well and deviation surveys for Red Sky and Figure 3.7 shows a 3D view of all 7 horizontal wells.

Table 3.2. Details of wells analyzed in the Red Sky survey.

Well Name	TVD (ft)	MD (ft)	Easting (USft)	Northing (USft)	Kelly Bushing (ft)
RS-NELSON_156_-91-1423H-1	9241	19041	1518171.45	494191.35	2250
RS-APELESE-156-91-1522H-1	8508	18128	1512916.76	494308.35	2278
RS-BLACK_STONE-156-911011H-1	8690	19503	1512955.82	499910.76	2303
RS-F-NELSON_156-91-2413H-1	8400	19199	1527077.32	484326.64	2218
RS-HOWELL-156-91-1207H-1	8400	19053	1523645.01	499728.63	2263
RS-STATE_B-156-91-1609H-1	7560	11765	1512019.76	489946.25	2260
RS-VEDAA-156-91-0336H-1	9647	13038	1513870.70	500417.63	2295

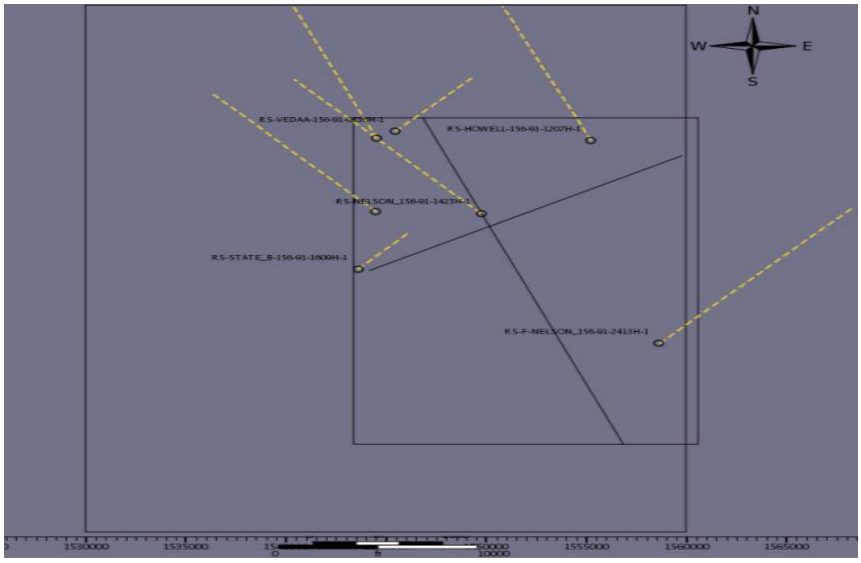

Figure 3.6. Base map view of Red Sky wells with deviation surveys displayed as broken yellow lines (2D lines as solid black lines).

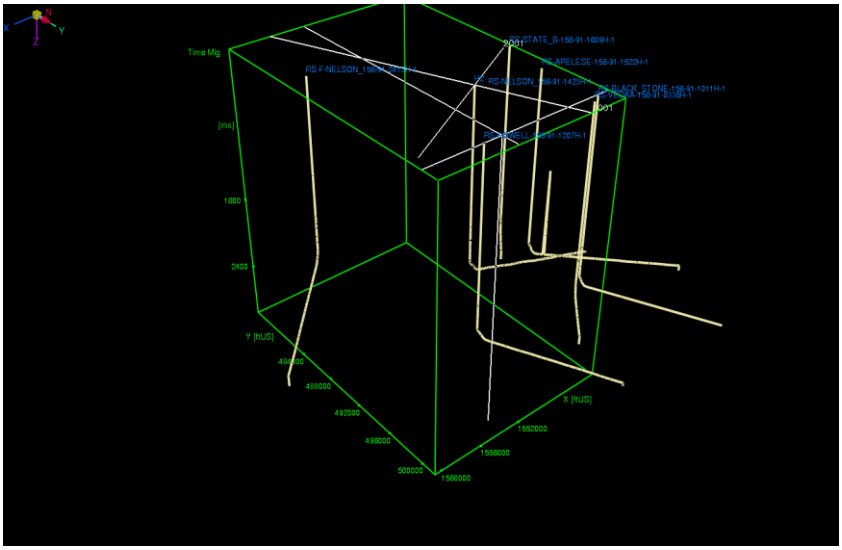

Figure 3.7. 3D view of Red Sky horizontal wells (in time domain).

3.5 Red Sky seismic survey

The seismic survey was acquired in October, 2008. Two 2D lines were shot and are named line 1001 and line 2001. Line 1001 is about 8km (5 miles) long while 2001 is 5.5km (3.5 miles) long. Both lines have shot intervals of 110 feet and receiver intervals of 55feet. As a result, the CMP interval is 55 feet. More details of Red Sky 2D survey is provided in Table 3.3.

Table 3.3. Acquisition parameters for 2D Lines 1001 and 2001 in Red Sky survey.

Line Name	Line Length (ft.)	# of Shots	# of Recs	# of CMPs	Min/Max Offset (ft.)	Line Azimuth/Orientation	Replacement Velocity (ft./s)
1001	26, 899	56	86	973	55/26,757	157.83/ NW-SE	7000
2001	18,088	65	30	652	55/17,912	240.13/NE-SW	7000

Details of the processing of the seismic data are illustrated in Chapter 4 and the corresponding analysis and interpretation are provided in Chapter 5. Figure 3.8 shows a Google Earth image of the Red Sky survey as well as an XY coordinate plot of the 2D lines.

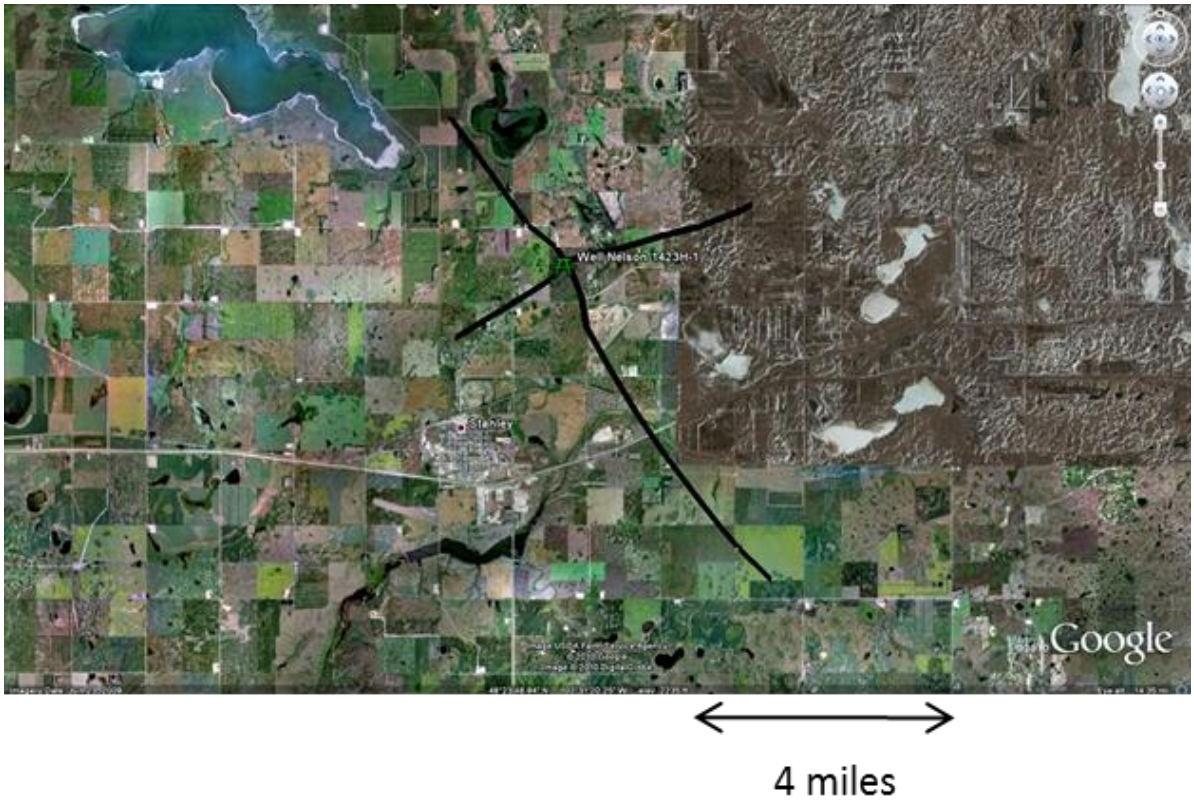

Figure 3.8. Google Earth image of Red Sky seismic survey lines. Well RS-NELSON_156_-91-1423H-1 is at the point where the two lines intersect.

Chapter 4

Red Sky data preparation and processing

4.1 Introduction

The seismic processing technique employed for the Red Sky survey was what could be termed as an industry standard seismic processing. With the exception of residual moveout analysis carried out in the analysis stage (described in Chapter 5), most of the processes were mundane. However, a lot of care was taken to preserve true amplitudes and to all the same enhance reflectors.

Details of the two shot lines were provided in Table 3.3; altogether, there are 265 shots on line 1001 at 110-foot intervals and 486 receivers at 5-foot intervals. Line 2001 has 179 shots at 110-foot intervals with 330 receivers at 55-foot intervals. For every shot, all receiver channels on both 2D lines were open, i.e., for a shot along 1001, receivers on 2001 were also open to record the signal. This could help map out a rough 3D surface or be used to compute a "poor man's 3D survey". Figure 4.1 shows a raw shot gather from line 2001 and Figure 4.2 is the

corresponding FK spectrum. Both figures show a frequency range of 10 to 110 Hz for the raw data. Other facts include: direct arrival velocity of 6300 feet/s, refracted arrival velocity of 7500 feet/s, ground roll velocity of 1900 feet/s which eventually lead to a statics replacement velocity of 7000 feet/s.

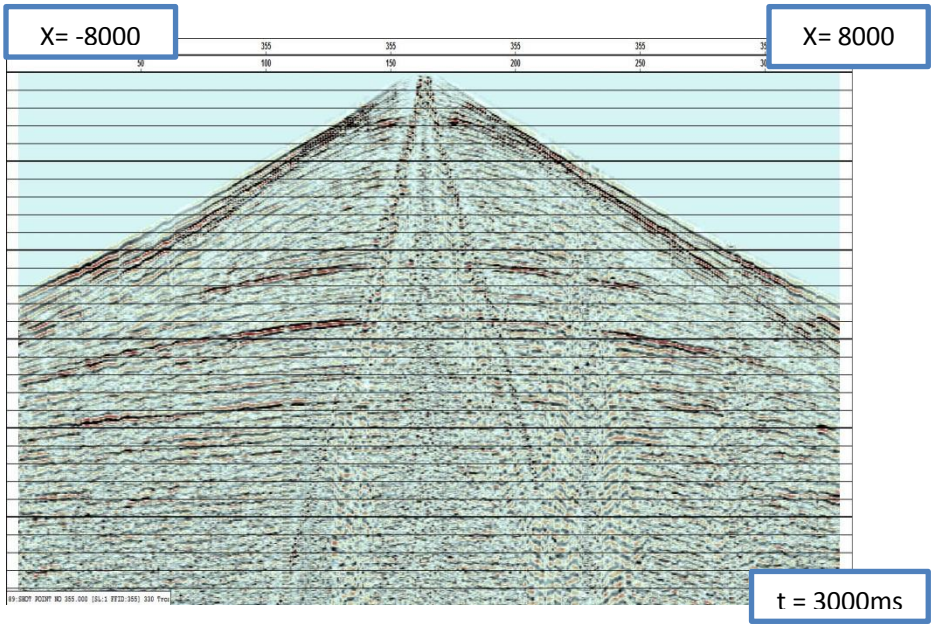

Figure 4.1. Raw shot gather from line 2001.

To attenuate unwanted signals in the data and to optimize the Red Sky survey for anisotropic investigation, a data processing workflow was established. The processing flow included, among others, component separation, first break picking and surface consistent deconvolution. The processing flow was designed to minimize processing steps and so keep the seismic data unblemished. Also

necessary noise attenuation techniques were incorporated to effectively attenuate noise at all levels. Figure 4.3 shows the processing flow for the Red Sky survey.

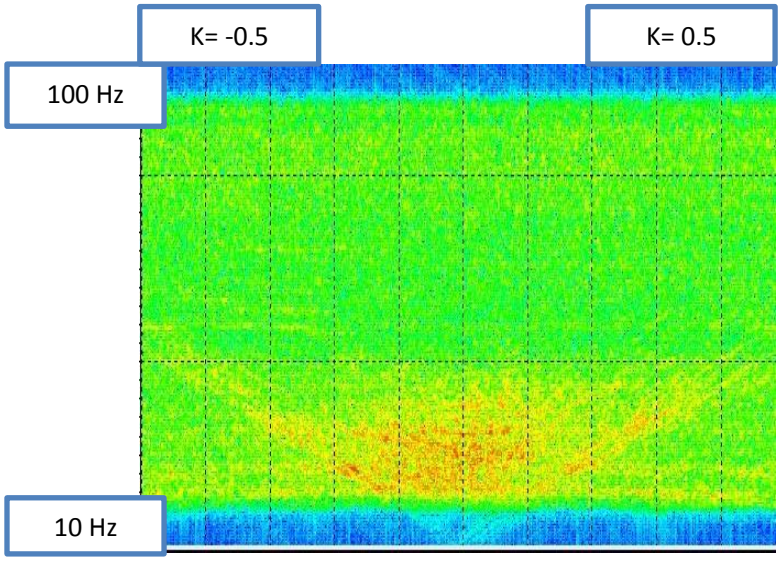

Figure 4.2. Corresponding FK spectrum from shot gather displayed in Figure 4.1.

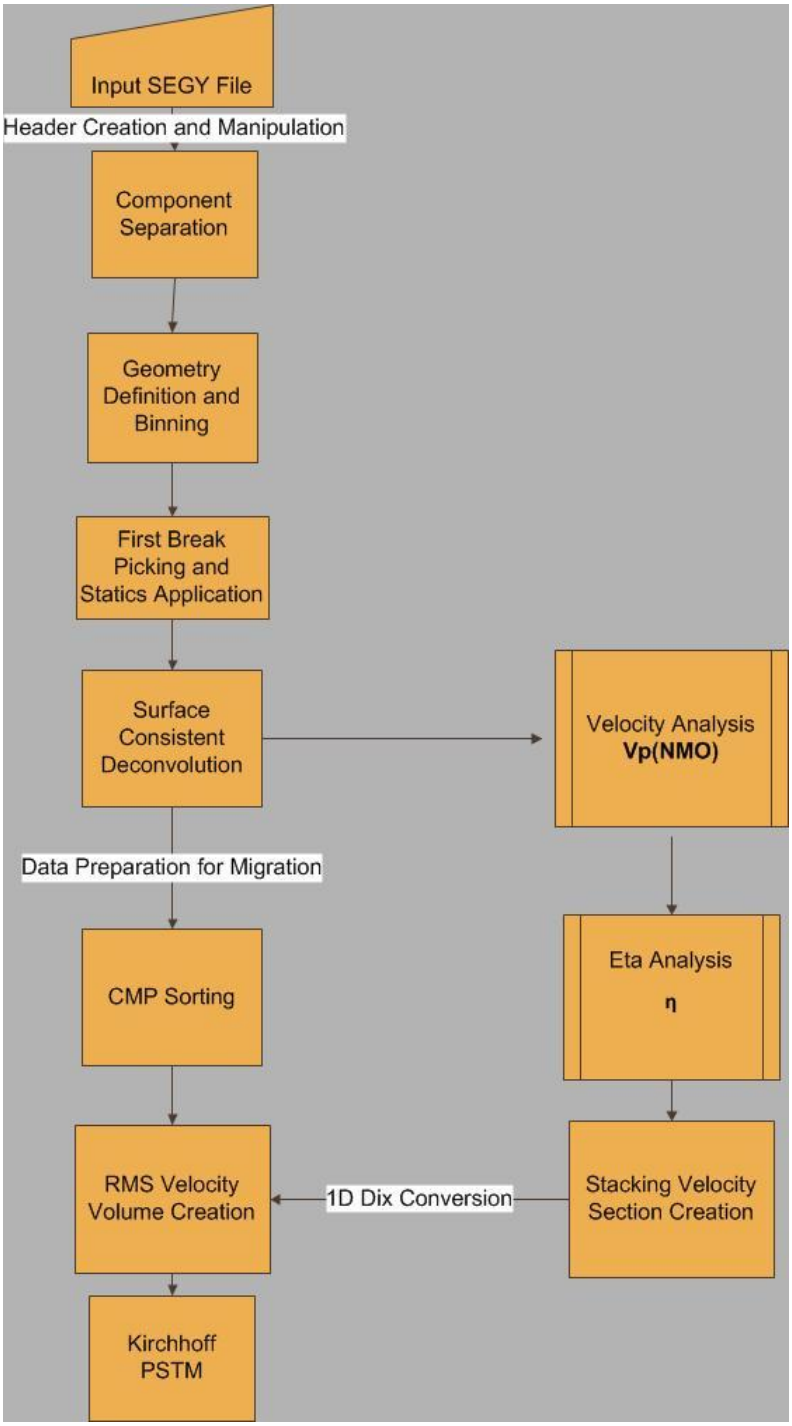

Figure 4.3. Processing flow diagram for Red Sky seismic survey.

4.2 Geometry definition and component separation

4.2.1 Component separation

The Red Sky survey was acquired as a 2D 3C survey. For every receiver location, three types of receivers were placed, which meant there are three traces per receiver location. Also, all receivers were recording for all shots. This meant that when shots were being taken for line 1001, receivers in line 2001 were open and were recording. This could add an additional azimuthal entity to the data or it could be used to produce a low resolution 3D. However, in this project we are least interested in this offline shooting and the extra data had to be deleted. Figure 4.4 shows a raw shot gather before separation. Note the offline shot to the right. Also, this shot gather contained all three traces per receiver location.

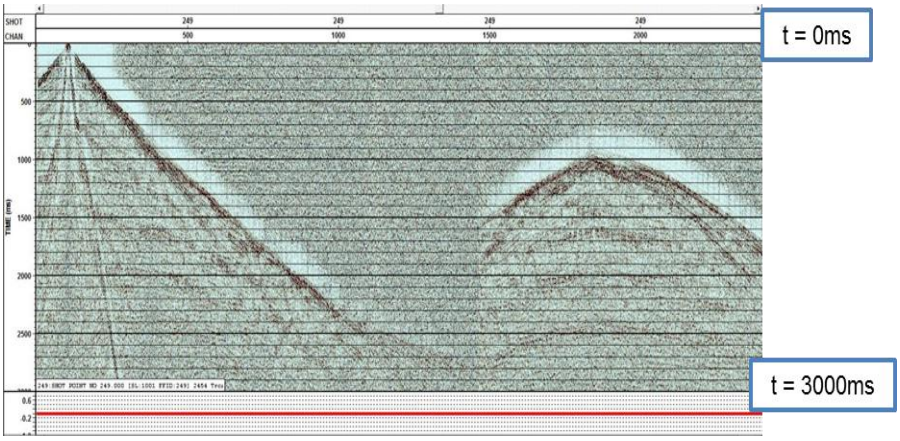

Figure 4.4. Raw shot gather before component separation from line 1001.

In Figure 4.5, open receiver geometry is demonstrated as a function of the shot location. At shot locations 1, 2, and 3, it can be seen that receiver response varies on both lines 1001 and 2001.

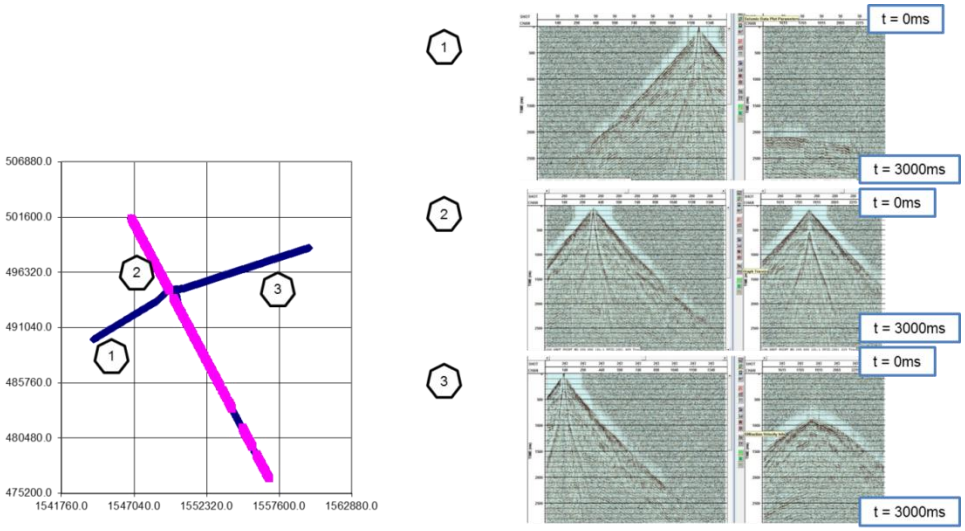

Figure 4.5. Geophone response from lines 1001 and 2001, showing open receivers on both 2D lines.

We deduced that using both sets of data might have been problematic. Reflections would have been out-of-phase and it would have been difficult to identify individual events on stacking. As a result, “out of line” traces were deleted before the proper component separation began.

The actual component separation was done in VISTA processing software using predefined segy headers. At byte location 208, the sensor type for each trace was given. A value of 6 means the vertical component (Z) while 7 is the radial

component (X) and 8 is the transverse component (Y). The VISTA job flow for the component separation is shown in Figure 4.6. After separation, all components of the segy file were in separate files. Figure 4.7 shows a shot gather after separation.

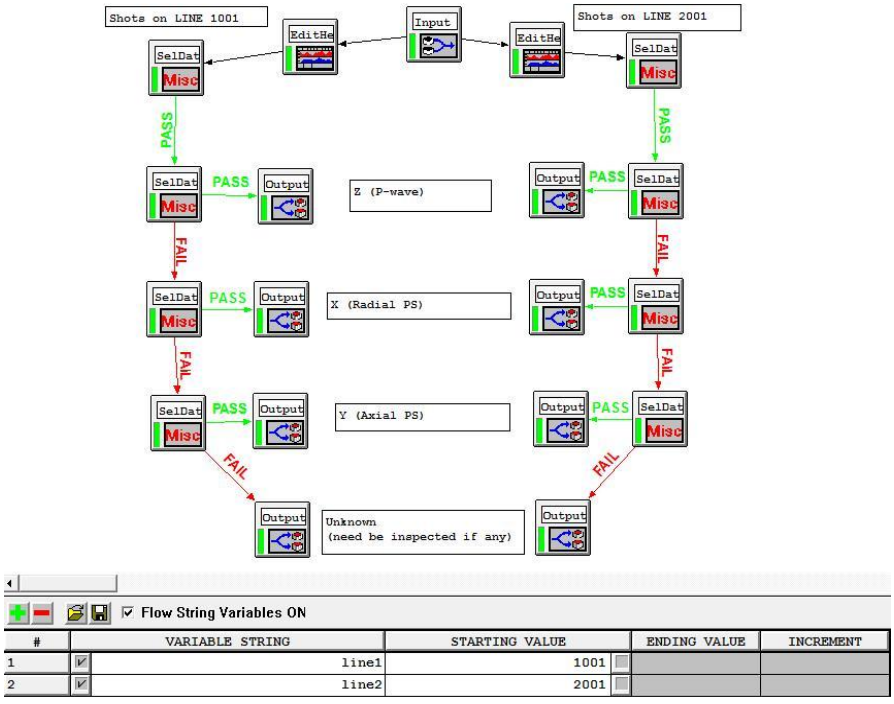

Figure 4.6. Job flow for component separation in VISTA software.

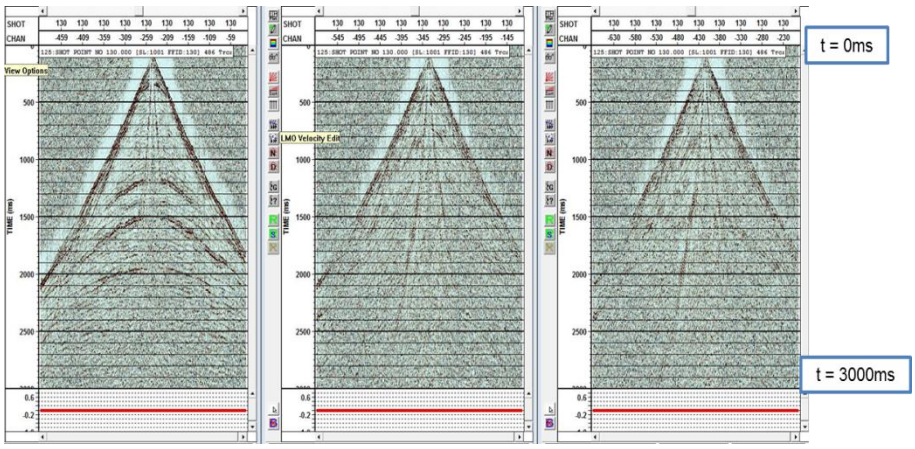

Figure 4.7: Raw shot gathers after separation. a) Z or vertical component; b) X or radial component; and c) Y or transverse component.

4.2.2 Geometry definition

Geometry for both lines 1001 and 2001 was defined in a supplied SPS file. The geometries were defined as crooked line geometry. Figure 4.8 shows line 1001 and the defined crooked line geometry. The Xline parameter was made wider so as to capture CMPs that might fall out of the 2D line.

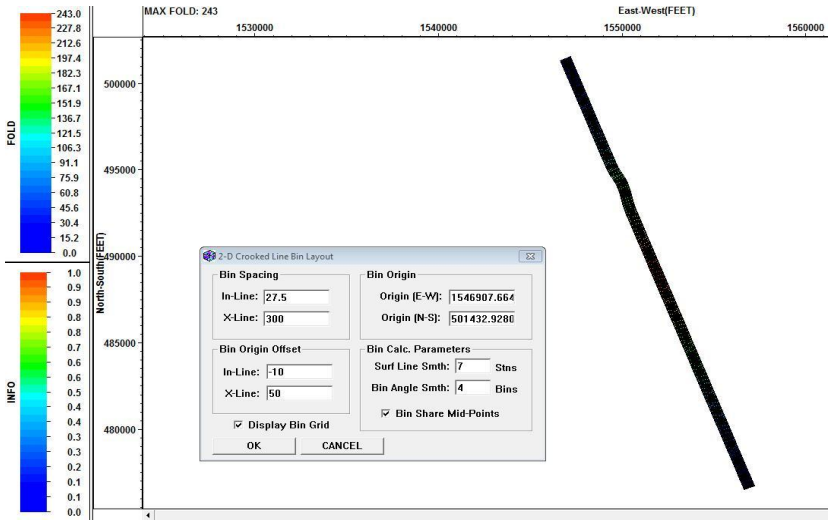

Figure 4.8. Line 1001 and defined crooked line geometry (maximum fold = 243).

A zoom of the geometry plot for Line 1001 shows the actual position of shots and receivers as well as midpoints. In Figure 4.9, red squares represent shot position, blue crosses represent receiver position and black dots represent CMP locations.

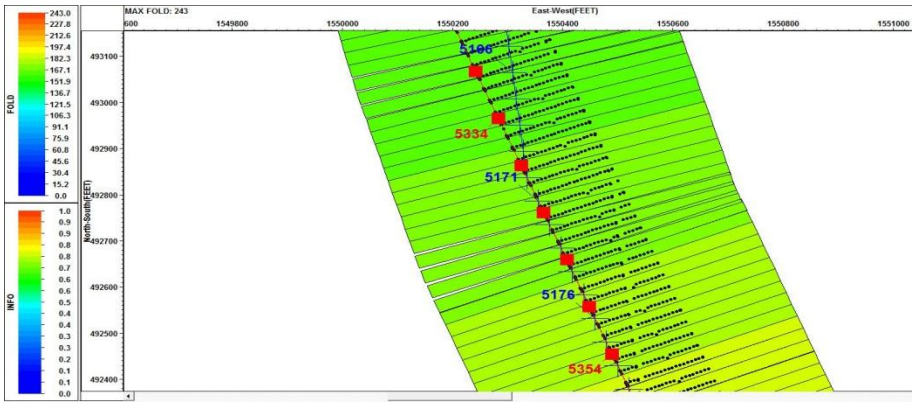

Figure 4.9. Zoom of geometry view on line 1001. Red squares represent shot position, blue crosses represent receiver position and black dots represent CMP locations.

4.3 First break picks and statics correction

4.3.1 First break picks and QC

First arrivals were auto picked on both lines 1001 and 2001. The search window was about 3000ms while the sliding window was about 75ms. These parameters were chosen after careful testing and experimentation. Figure 4.10 shows a first break pick display for Line 1001. The first break picks are in blue. A QC of the first break picks is also shown in Figure 4.11.

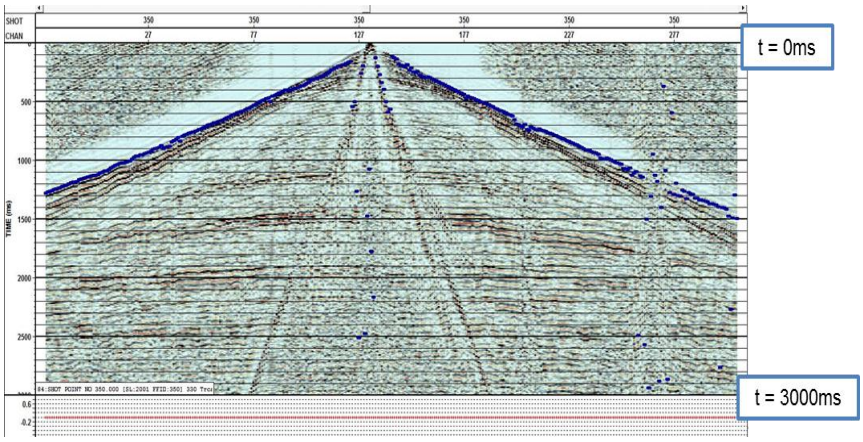

Figure 4.10. Raw shot gather from line 1001 showing first break picks.

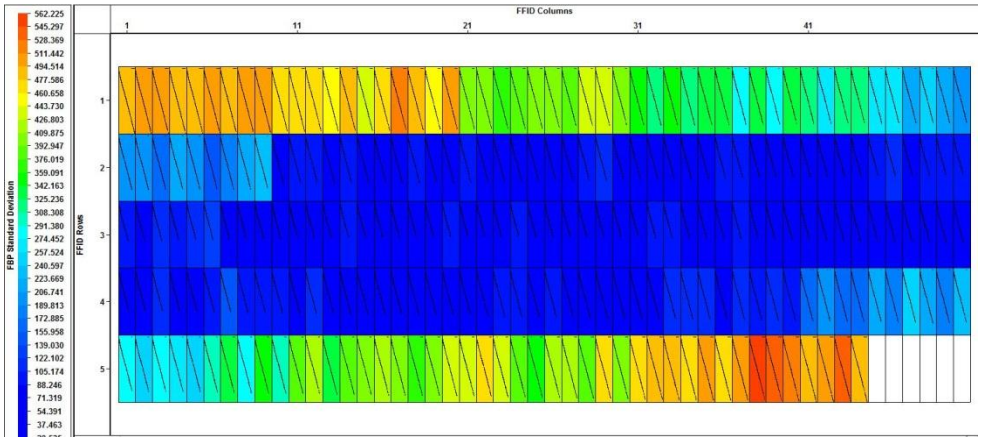

Figure 4.11. QC view for all first break picks on line 1001. Here picks are plotted against offset and each box represents a shot gather.

4.3.2 Elevation and refraction statics

Shot and receiver elevation values were supplied from an SPS file. The combination of picked first break and elevation values provided the input for statics correction. Shot and receiver elevation values ranged from 2150 to 2280 feet. above sea level. As a result, fixed datum was set at 2300 feet. Figure 4.12 shows datum elevation position with reference to source and receiver elevations.

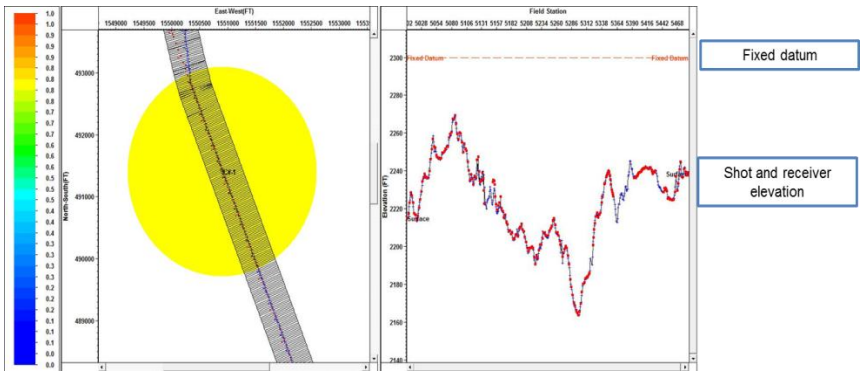

Figure 4.12. Statics computation view for Line 1001 showing fixed datum and shot and receiver elevation.

To determine replacement velocity to be used for processing, the first breaks were analyzed with reference to supplied shot and receiver elevation. Three layers were defined and background replacement velocity was fixed at 7000 feet/s; weathering velocity was also fixed at 2400 feet /s. Figure 4.13 shows statics computation showing refracted arrival velocities of 6500, 7200 and 7800 feet/s for three defined layers. Statics correction values were stored on the trace headers and applied before stacking.

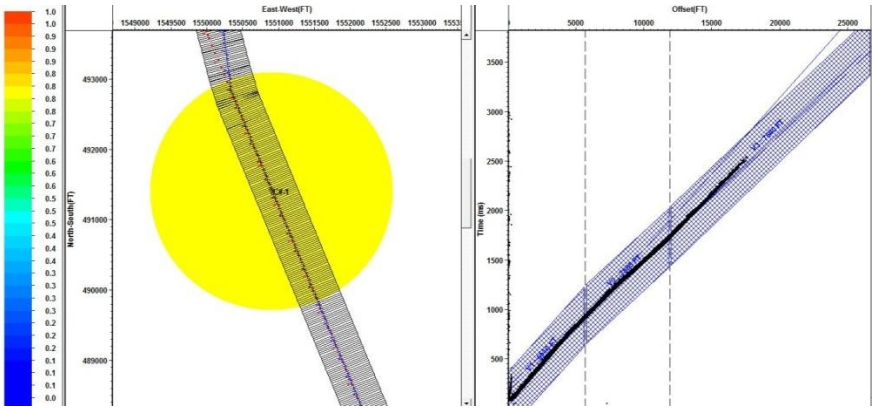

Figure 4.13. Statics computation view showing refracted arrival velocities of 6500, 7200 and 7800 ft/s.

4.4 Surface-consistent deconvolution

For surface-consistent deconvolution to be performed, a time window for SCAC computation was defined. This time window was between 1000 and 1500ms. SCAC parameters were computed from shot, receiver, offset and CMP domains. Surface consistent predictive deconvolution was then applied with an analysis gate of 250 ms and 1% white noise added. Figure 4.14 shows a shot gather from line 2001 before and after SC deconvolution.

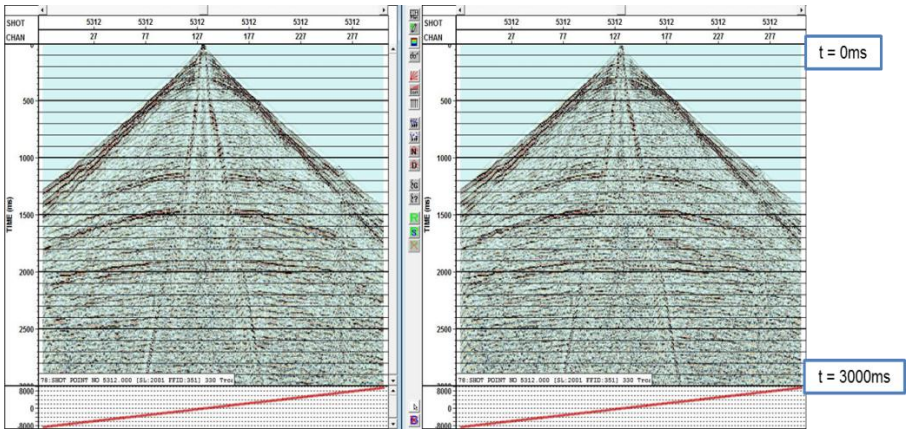

Figure 4.14. Shot gather from line 200.1 a) before SC deconvolution; b) after SC deconvolution.

The changes on the shot gathers after SC deconvolution are subtle but significant. Figures 4.15 and 4.16 show power spectra off all traces in the shot gather. Notice that the power spectra are more regularized in Figure 4.16 (after SC deconvolution) than in Figure 4.15 (before SC deconvolution). Also one can see that before SC deconvolution, far offset traces seem to be losing frequency content but these frequencies content have been restored after deconvolution.

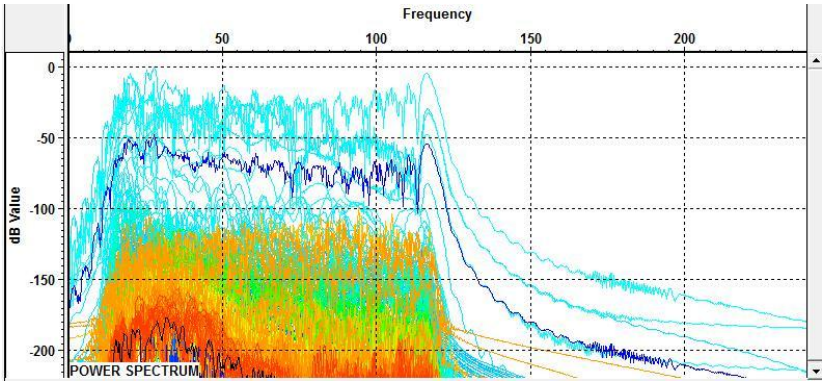

Figure 4.15. Power spectrum of all 265 traces from a shot gather on 2D line 2001 before SC deconvolution; bluish colors represent near offset traces and yellow/reddish colors are far offset traces.

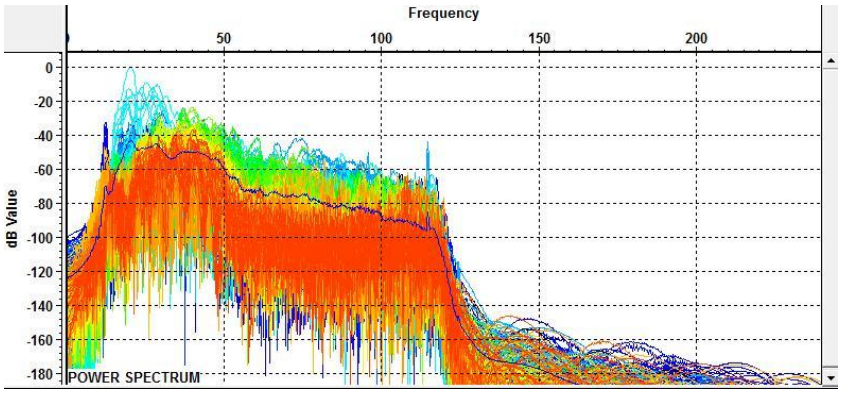

Figure 4.16. Power spectrum of all 265 traces from a shot gather on 2D line 2001 after SC deconvolution; bluish colors represent near offset traces and yellow/reddish colors are far offset traces.

4.5 Shot domain noise attenuation

4.5.1 Band pass filtering and amplitude despiking

A band pass filter of 8, 16, 48, and 64 Hz was applied to remove high frequency noise introduced by deconvolution and low frequency direct arrivals. An amplitude despiking module was also added to remove noise bursts and attenuate and air blast. Figure 4.17 shows a shot gather before and after band pass filtering and amplitude despiking, it also shows a difference plot.

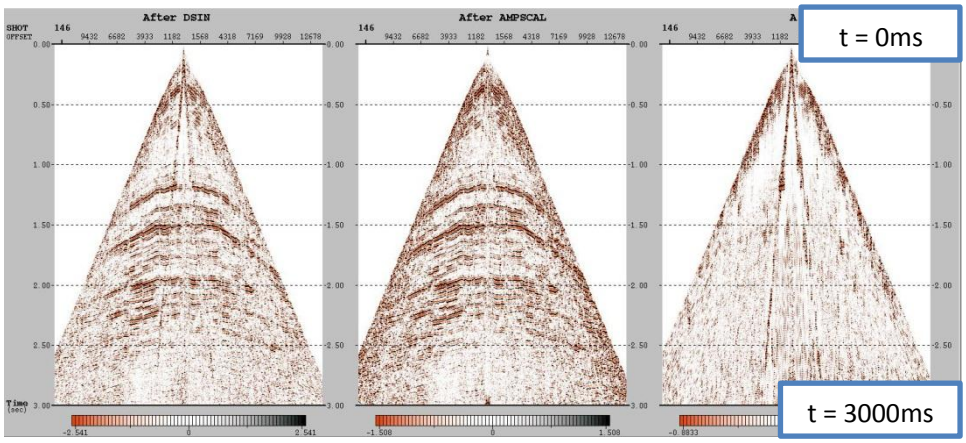

Figure 4.17. Shot gather. a) before band pass filtering and amplitude despiking; b) after band pass filtering and amplitude despiking; c) difference plot A-B.

4.5.2 Random noise attenuation and trace balancing

A time-frequency domain noise attenuation module was introduced to further remove random noise and balance traces. This technique also eliminates remaining direct arrival in the data. Figure 4.18 shows the same shot gather before and after time-frequency domain attenuation and also a difference plot.

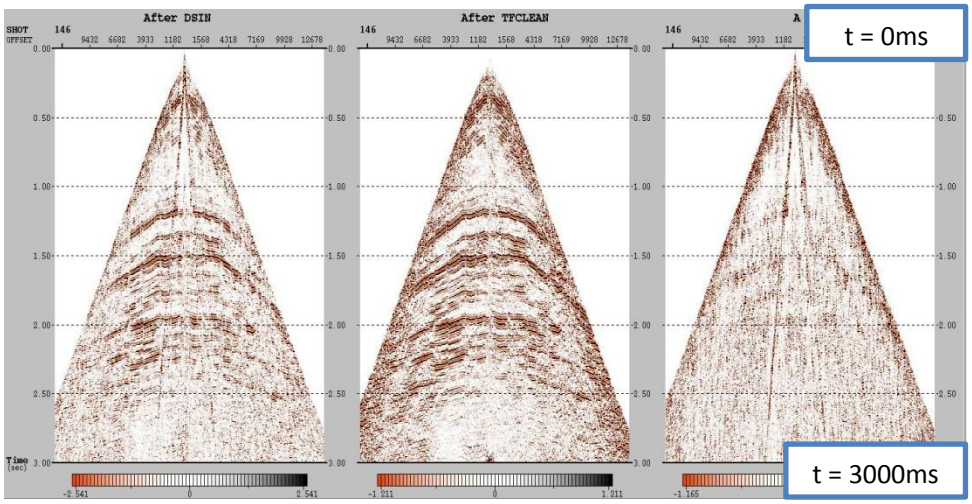

Figure 4.18. Shot gather. a) before time-frequency domain attenuation; b) after time-frequency domain attenuation; c) difference plot A-B.

4.5.3 FX deconvolution

The data was finally passed through an FX deconvolution module to enhance signals and attenuate random noise. Figure 4.19 shows shot number 146 before and after FX deconvolution and a difference plot.

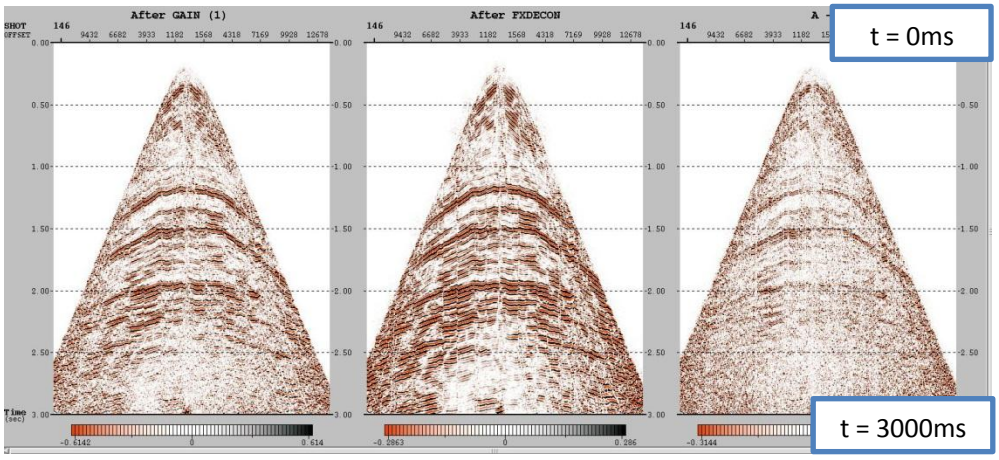

Figure 4.19. Shot gather. a) before FX deconvolution; b) after FX deconvolution; c) difference plot A-B.

4.6 CMP Sorting, velocity analysis and migration

Data were sorted to CMP after noise attenuation. Preliminary velocity analysis also commenced. Stacking velocities were picked every 10 CMPs (550 feet or 0.1 mile interval). Altogether there were 50 vertical functions for line 1001 and 35 vertical functions for 2001. Velocity values ranged from 6400 to 13000 feet/s. Figure 4.20 shows the stacking velocity analysis window (Paradigm Geodepth software) on CMP 400 on line 1001. Notice the residual curvature at about 1100ms due to the Greenhorn Formation. This residual moveout is analyzed in detail in Chapter 5. Figure 4.21 shows a final stacking velocity section for line 1001.

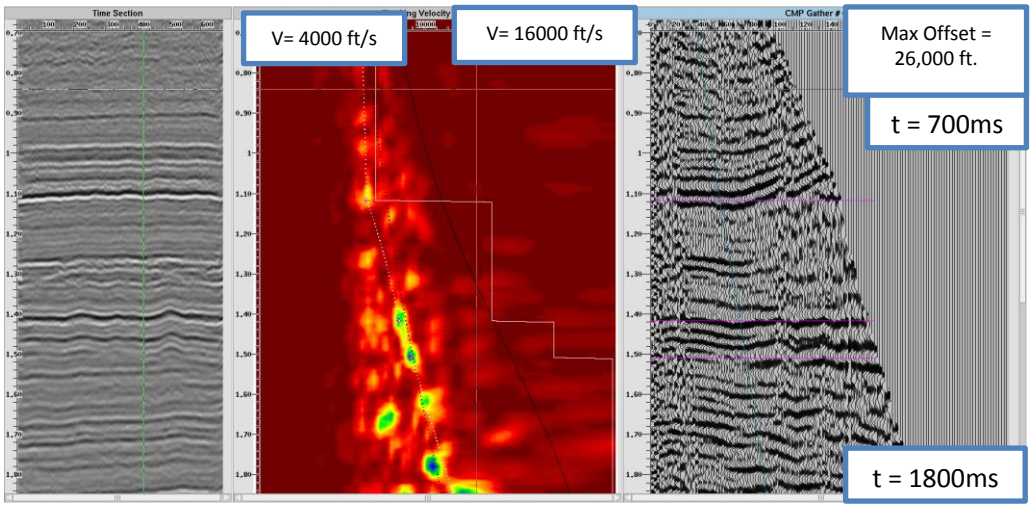

Figure 4.20. Stacking velocity analysis display for CMP 400, line 1001 (Paradigm Geodepth software). a) CMP stack section; b) stacking velocity semblance plot; c) CMP gather with maximum offset of 26,000 feet.

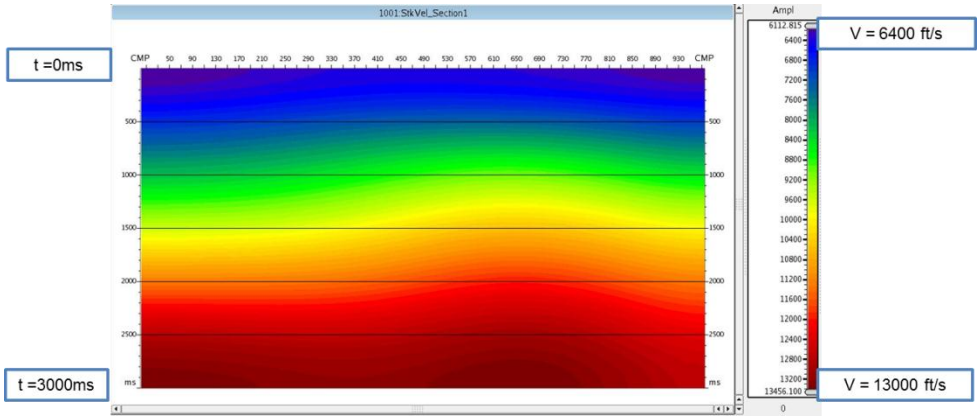

Figure 4.21. Final stacking velocity section for line 1001.

Stacking velocities were converted to RMS velocities using 1D Dix equation and were fed into a Kirchhoff pre-stack time migration application. Figure 4.22 shows a final migrated image of line 1001. Figure 4.23 shows a zoom on the final migrated section.

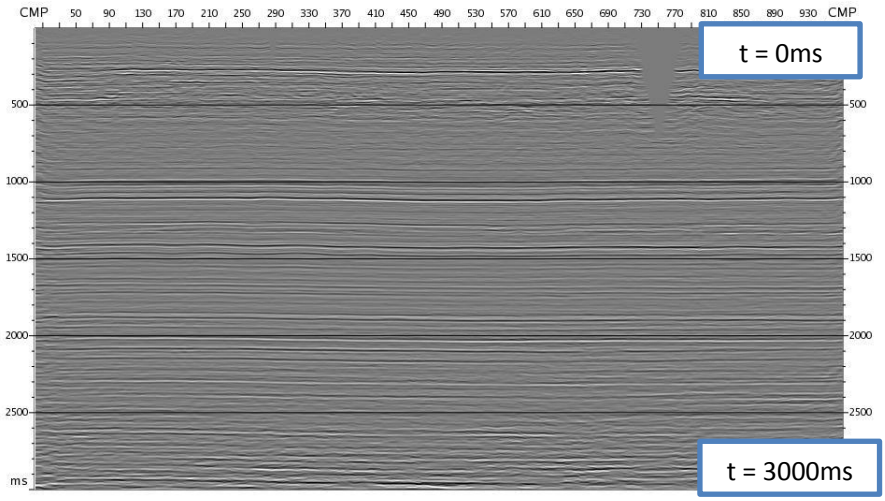

Figure 4.22. Final pre-stack time migrated image of line 1001.

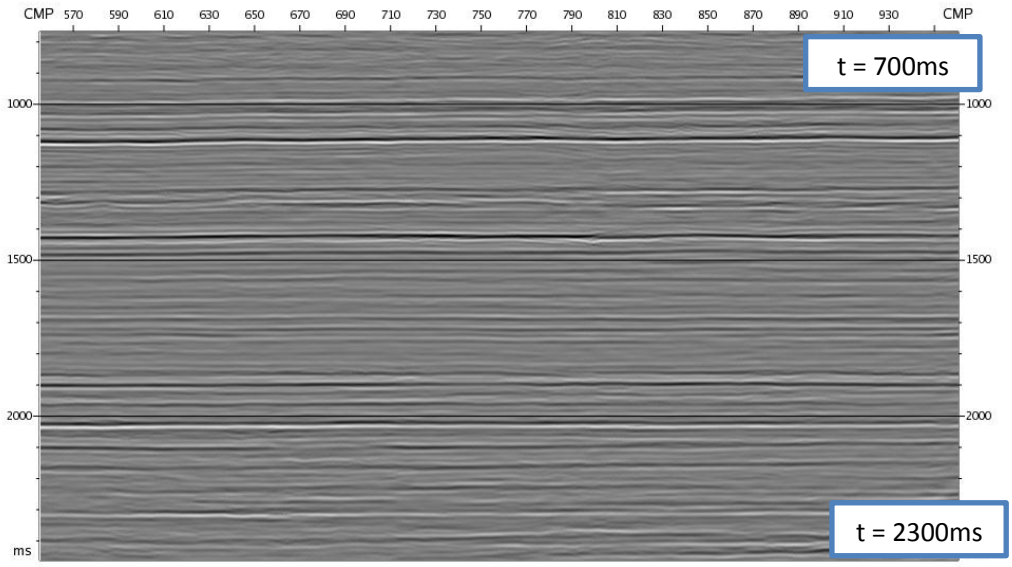

Figure 4.23. Zoom on Kirchhoff time migrated section, Greenhorn Formation is at 1100ms and Bakken formation at 1900ms.

Chapter 5

Results and analysis

5.1 Introduction

The Mississippian-Devonian Bakken Formation is an attractive petroleum exploration target with 3 to 5.3 billion barrels of technically recoverable oil (USGS, 2008). Typically horizontal drilling and hydraulic fracturing are used to exploit this vast resource. Seismic imaging can help identify high pay zones and improve overall drilling success.

In this chapter, we correlate and compare calculated shale volume derived from gamma ray logs to residual moveout estimated from seismic gathers. Since the existence of open vertical natural fractures can be a good indicator of hydrocarbons in the Bakken petroleum system, field seismic data from the Williston Basin were compared to laser-etched physical models with specific fracture patterns. Fracture density and orientation were varied in these physical models to help quantify and explain anomalies in field data. Also, seismic derived anisotropic parameters were compared to ultrasonic core measurements.

Since non-hyperbolic moveout on seismic data is sometimes attributed to anisotropy, our project aims to quantify seismic derived anisotropy by comparing with shale volume and core data from the Williston Basin. Assumptions of hyperbolic NMO used for seismic processing becomes inadequate at far offsets; while this may constitute an imaging problem, it is also invaluable for estimating anisotropic parameters from seismic data.

Mostly seismic travel time information is used to adequately focus the final seismic image. Recent advances in seismic anisotropy have, however, extended this travel time information to help identify fractures and faults and sometimes serve as a lithology indicator. Shales are intrinsically anisotropic and they behave as an anisotropic media with a vertical axis of symmetry (VTI). Based on these assumptions, we were able to infer that seismic residual moveout could be attributed to shale formations provided we had well data to verify. The extent to which this statement is true is the subject of this investigation. In essence the question is "how reliable is seismic residual moveout analysis as a lithology indicator?". As is the case with most seismic reflection projects, the quality of reflectors (seismic data quality) and the quality of data preparation (seismic processing) determines the success of the project. To directly invert anisotropic parameters and lithology from seismic travel times requires good quality seismic data and skillful processing. The data used in this project were courtesy of the Hess Corporation and the North Dakota Industrial Commission.

5.2 Objectives

The main intention of this particular study was to help identify and categorize productive zones in shales; in other words, our goal was to diagnose seismic characteristics associated with better productivity in Bakken Formation

Factors affecting productivity in shale plays may include the following:

1) Hydrocarbon potential (from regional geologic reports);

2) Presence of fractures or faults to serve as porosity for hydrocarbon accumulation;

3) Rock brittleness to enable more effective hydraulic fracturing to increase permeability;

4) Stress anisotropy (direction of preferred rock breakage).

These factors may manifest as the following seismic characteristics or attributes:

1) Seismic anisotropy due to the presence of shales and open vertical fractures;

2) High Young's modulus and low Poisson ratio diagnostic of rock brittleness.

Figure 5.1 is a plot of calculated Young's modulus E against poisson's ratio $\boldsymbol{\sigma}$ (derived from Vp, Vs. and ρ, using the formulas below) across a horizontal well;

$$\boldsymbol{\sigma} = \frac{\left(\frac{V_p}{V_s}\right)^2 - 2}{2\left(\frac{V_p}{V_s}\right)^2 - 2} \qquad (5.1)$$

$$E = 2\mu(1 + \boldsymbol{\sigma}) \qquad (5.2)$$

3) Shear wave splitting leading to incremental mistie between fast and slow converted wave sections Lynn and Thomsen, (1990);

4) Amplitude and waveform effects (difference in amplitude of event in slow and fast C-wave sections) Mueller, (1992).

Here we only focused on the first manifestation due to the presence of shales and open vertical fractures (seismic anisotropy) and compared these results to a controlled laboratory experiment using laser-made fracture models.

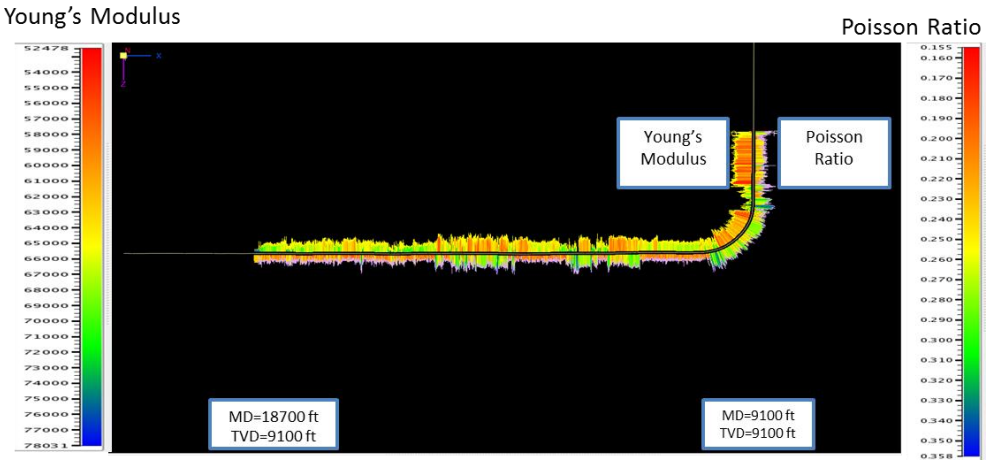

Figure 5.1. Plot of calculated Young's Modulus against Poisson's ratio across a horizontal well (Well Name: RS-NELSON_156_91-1423H-1).

5.3 Residual eta ($\boldsymbol{\eta}$) analysis

Preliminary velocity analysis in section 4.6 suggests that there is considerable residual delay on CMP gathers after NMO correction. Figure 4.20 showed a velocity analysis window on CMP 400 for line 1001. From this figure at about 1100ms (from the Greenhorn Formation), notice the residual curvature despite the application of the correct and adequate NMO velocity. This residual curvature appeared consistently around the Greenhorn Formation and the Bakken system (Lodgepole, Bakken, and Three Forks Formations).

Eta is a measure of the non-hyperbolic moveout correction needed to accurately flatten events on gathers when hyperbolic NMO/stacking velocities leave a residual curvature. Eta is sometimes a measure of the anisotropy in a formation. While eta can be purely isotropic, the geology and gamma ray logs reveal an abundance of shale at these formations which suggest a considerable amount of anisotropy might be involved in these residual moveouts. One of the objectives of our study was to quantify non-hyperbolic moveout with the help of physical models.

$$t^2(X)=t_0^2+\frac{X^2}{V_{nmo}^2}-\frac{2\eta X^4}{V_{nmo}^4 t_0^2} \tag{5.3}$$

$$\eta = \frac{\varepsilon-\delta}{1+2\delta} \tag{5.4}$$

where

t is total travel time and

t_0 is zero offset two way travel time and $\boldsymbol{\eta}$ is eta.

Eta analysis was also performed on every 10^{th} CMP (550 ft. or 0.1 mile interval) on both lines 1001 and 2001, with the initial mute removed. Eta analysis was carried out after CMP gathers were time migrated with Dix-derived RMS velocities. Figure 5.2 shows a simultaneous stacking velocity and residual eta analysis window on a CMP gather (Paradigm Echos software). Average residual eta estimates for the Greenhorn formation were 0.3 (Figure 5.3); for the Bakken Formation, they ranged from 0.05 to 0.2. Notice in Figure 5.2 events at far offset are flattened after eta picking. Figure 5.3 is a plot of the summed NMO velocity and residual eta vertical functions for line 1001 displayed beside the final P-wave migrated section.

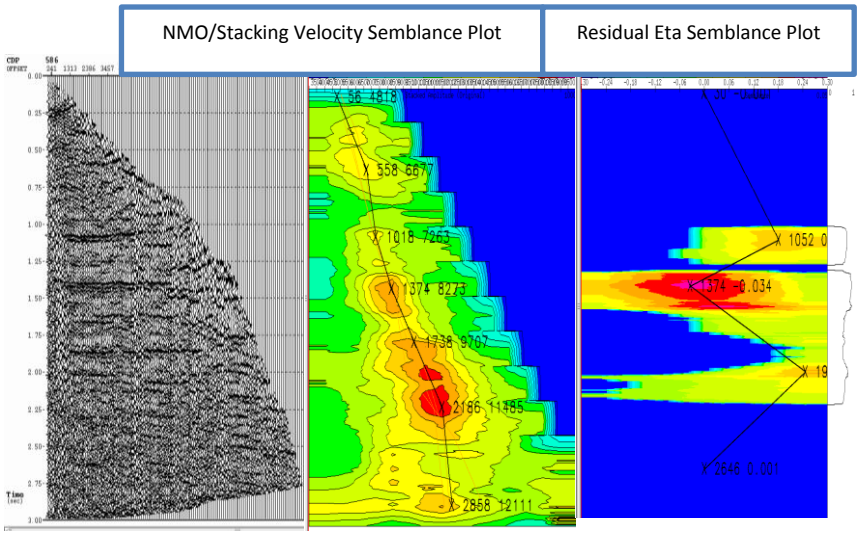

Figure 5.2. CMP Gather (Greenhorn Formation ~1100ms and Bakken Formation ~1850ms) with corresponding V(nmo) and eta semblance plots. The two numbers shown on each section are time-V(nmo) and time-eta pairs respectively.

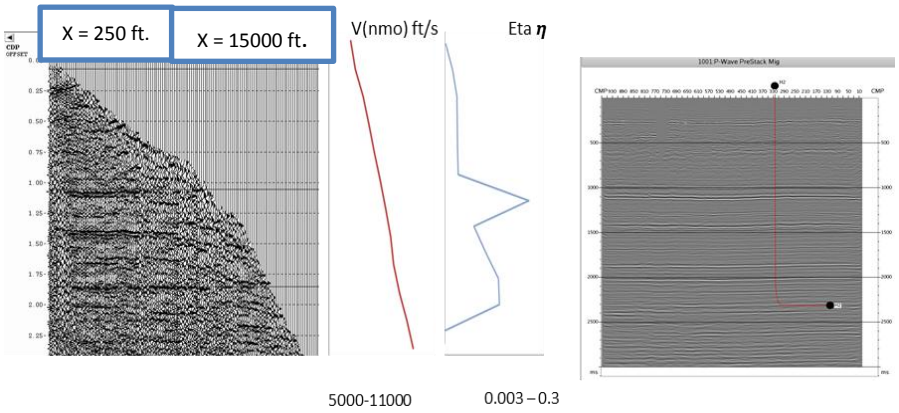

Figure 5.3. Average V(nmo) and eta values from a CMP gather displayed beside the CMP stack section.

Results show that residual $\boldsymbol{\eta}$ around the Greenhorn Formation was consistently around 0.3. At the Bakken Formation however, residual $\boldsymbol{\eta}$ results varied widely

and were sometimes negative. Figure 5.4 shows a final residual eta section for line 2001 (CMPs 250 to 400) with calculated shale volume log overlaid. Notice the area of high residual $\boldsymbol{\eta}$ also corresponds to an area of high shale volume (especially in the Greenhorn Formation). In Chapter 1, a study was undertaken to understand the influence of fracture orientation on seismic non-hyperbolic moveout. The result from Chapter 1 showed that for a non-VTI media, residual $\boldsymbol{\eta}$ is lower or even negative. However, for a perfect VTI media, residual $\boldsymbol{\eta}$ is the highest.

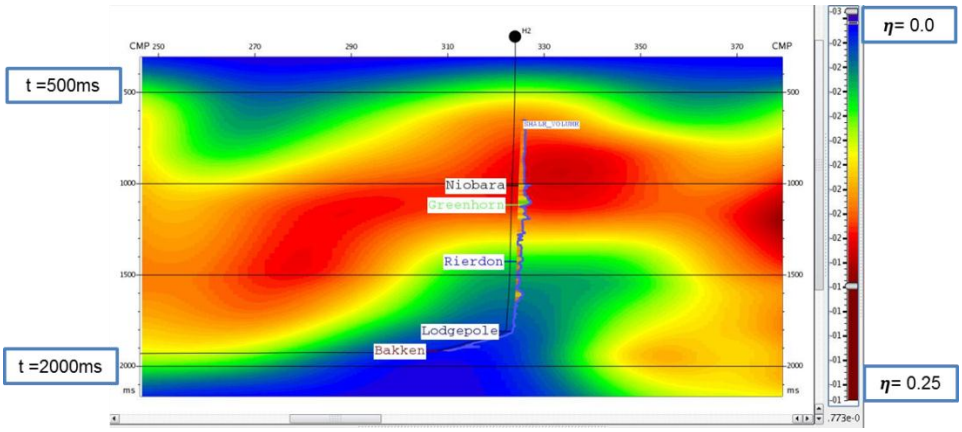

Figure 5.4. Final residual eta section for line 2001 (CMPs 250 to 400) overlaid with calculated shale volume log from well RS-NELSON_156_91-1423H-1.

5.4 Shale volume calculation

Shale volume was initially calculated for the whole well interval for all 7 wells. Since all rock types under investigation are older and more lithified (older than tertiary), non-linear equations were used:

$$I_{GR} = \frac{GR_{log} - GR_{min}}{GR_{max} - GR_{min}} \quad (5.5)$$

where I_{GR} = Gamma ray index

GR_{log}= gamma ray reading for formation,

GR_{min} = minimum gamma ray (clean sand or carbonate), and

GR_{max} = maximum gamma ray (shale).

Volume of shale was then calculated using the Steiber (1970) equation

$$V_{sh} = \frac{I_{GR}}{3 - 2I_{GR}} \quad (5.6)$$

Gamma ray readings for the Bakken Formation was about 800 API and for the Niobara (and Pierre) Formation they were about 300 API. The well was later divided into two segments and shale volume was calculated for each segment. The very high gamma ray reading at the Bakken may have been due to the high concentration of radioactive materials. Core data and previous geologic studies suggest the Greenhorn Formation is almost equally rich in shale but these shales may have less radioactive content. Here, however, we are concerned with the

effect of bulk volumes of shale on seismic wave propagation and not the type, radioactivity or organic content of the shales.

Figure 5.5 shows a gamma ray log with the calculated shale volume log from well NELSON_156_-91-1423H-1. Notice the high gamma ray and shale volume readings are in the Niobara-Greenhorn interval as well as in the Bakken Formation.

Figure 5.6 shows shale volume plotted on final Kirchhoff time migrated section. Notice the areas of high shale volume correspond to the Greenhorn Formation and the Bakken system.

The final shale volume calculation for Niobara to Greenhorn is from 40 to 60 % and in the Bakken formation it is 80%.

Results show that areas of high shale volume correspond to certain shaley formations. The Niobara to Greenhorn interval is particularly obvious and it displays an interval of about 1000 feet of high gamma ray (and shale volume) readings.

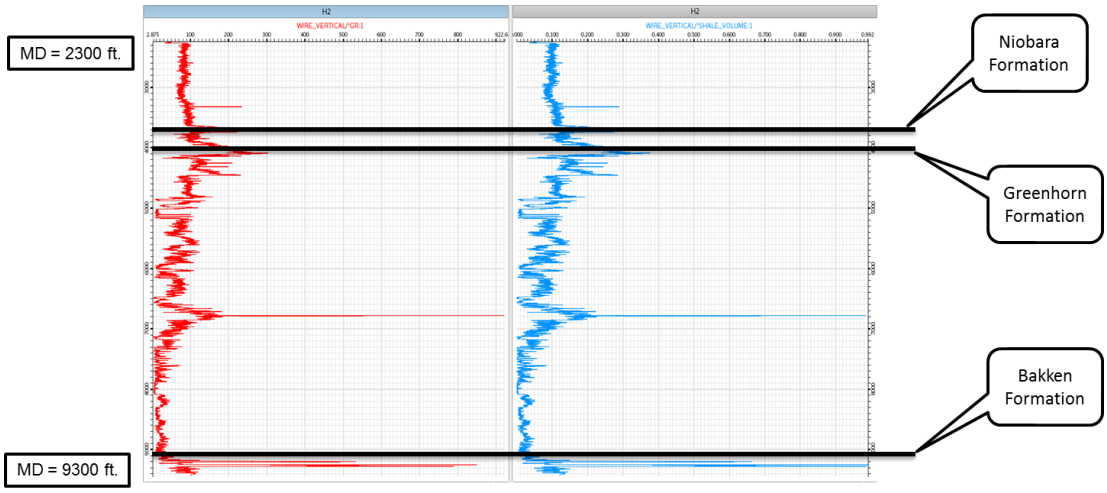

Figure 5.5. Gamma ray log with corresponding calculated volume of shale (Well: RS-NELSON_156_-91-1423H-1).

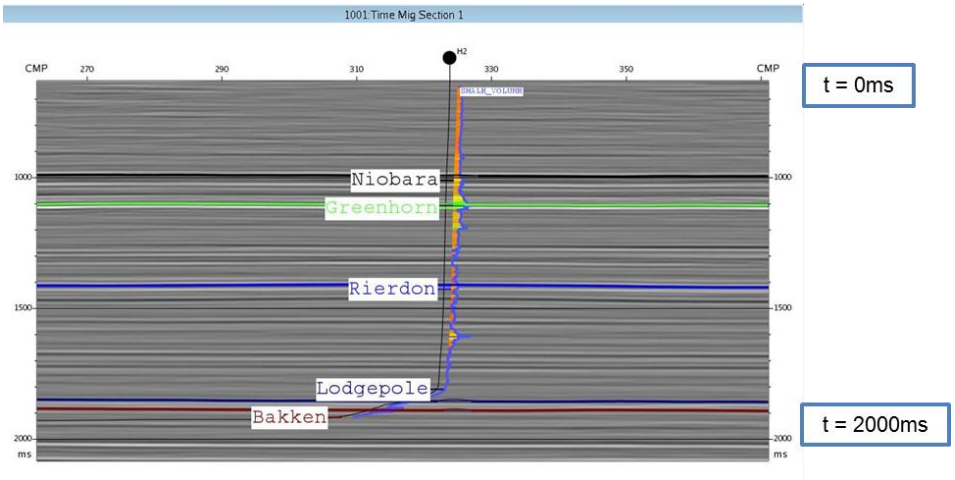

Figure 5.6. Calculated shale volume from well logs overlaid on a final migrated seismic section. Notice areas of high clay content correspond to the Niobara, Greenhorn and the Bakken Formations.

5.5 Previous core measurements (Jones and Wang, 1981)

Jones and Wang (1981) measured stiffness coefficients (described in section3.3) for Greenhorn shales. These results were inserted into Thomsen's (1986) equation to estimate Thomsen parameters and subsequently residual eta. The aim was to compare these anisotropic parameters with seismic derived parameters. Table 5.1 gives details of the estimated parameters.

Table 5.1. Estimated anisotropic parameters from Jones and Wang's (1981) experiment on Greenhorn shales.

Estimated ε	Estimated $\boldsymbol{\gamma}$	Estimated $\boldsymbol{\delta}$	Estimated $\boldsymbol{\eta}$
0.255	0.481	-0.051	0.341

Thomsen's (1986) equation for estimating anisotropic parameters is written as equations 5.7-5.9 and the Alkhalifah (1997) residual eta equation is written as equation 5.10:

$$\varepsilon = \frac{C_{11} - C_{33}}{2C_{33}} \tag{5.7}$$

$$\gamma = \frac{C_{66} - C_{44}}{2C_{44}} \tag{5.8}$$

$$\delta = \frac{(C_{13} - C_{44})^2 - (C_{33} - C_{44})^2}{2C_{33}(C_{33} - C_{44})} \tag{5. 9}$$

$$\eta = \frac{\varepsilon - \delta}{1+2\delta} \tag{5.10}$$

The estimated residual $\boldsymbol{\eta}$ from Jones and Wang's experiment agrees with the reading from seismic non-hyperbolic moveout measurements. Residual $\boldsymbol{\eta}$ analysis from seismic data shows a maximum $\boldsymbol{\eta}$ of about 0.3, while the estimated values from the Jones and Wang experiments are 0.341. These residual $\boldsymbol{\eta}$ (by Jones and Wang) act as constraints for traditionally less reliable seismic non-hyperbolic moveout measurements.

5.6 Mistie analysis

Time horizons/events were picked at particular formations on both lines 1001 and 2001. Processed VSP data were displayed side by side with the CMP stack section and desired formations were picked. This way the accuracy of the picks was ensured and errors due to picking were minimized. The objective was to compare these time horizons to TWT well markers and observe mistie in the time domain. The depth markers were converted to time using supplied time-depth curves. The defined formations are: the Niobara, Greenhorn, Dakota, Rierdon, Madison, BLS, Lodgepole and Bakken Formations. Figure 5.7 shows a processed VSP section supplied by the Hess Corporation from which time-depth curves were extracted. With the help of this time-depth curve, markers were able to be displayed in time and compared/calibrated to picked time horizons.

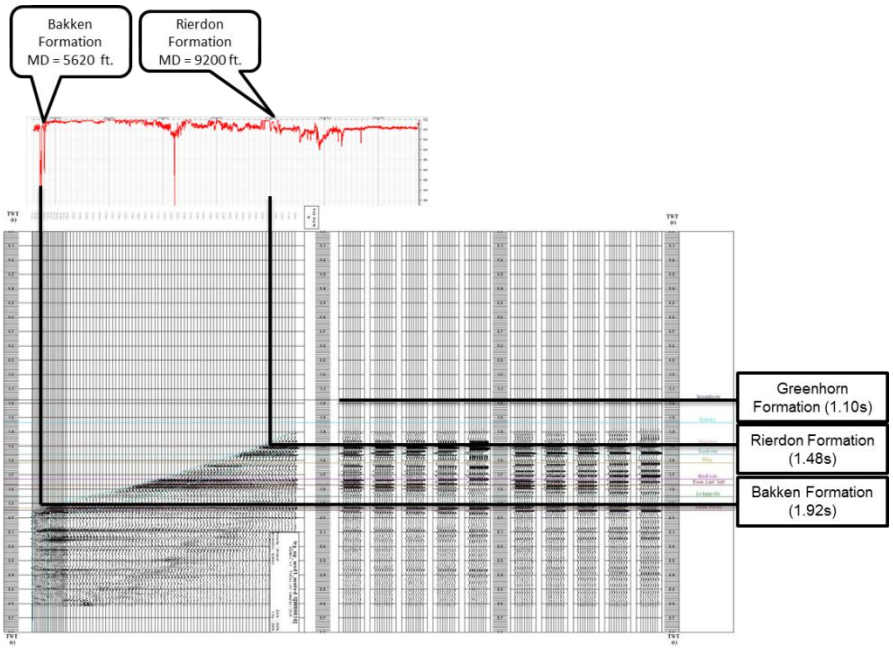

Figure 5.7. Processed VSP data displayed alongside gamma ray log from Red Sky survey area (data supplied by the Hess Corporation). This figure shows corridor stacks for all formations from Rierdon to Bakken with time and depth readings; however the VSP data does not image the Greenhorn formation.

A user-defined boundary was also drawn around the 2D lines so as to accommodate all wells for the purpose of the mistie analysis. Figure 5.8 shows picked horizons on the seismic section for line 1001 from CMP 250 to 450 (Well NELSON_156_-91-1423H-1 is also displayed).

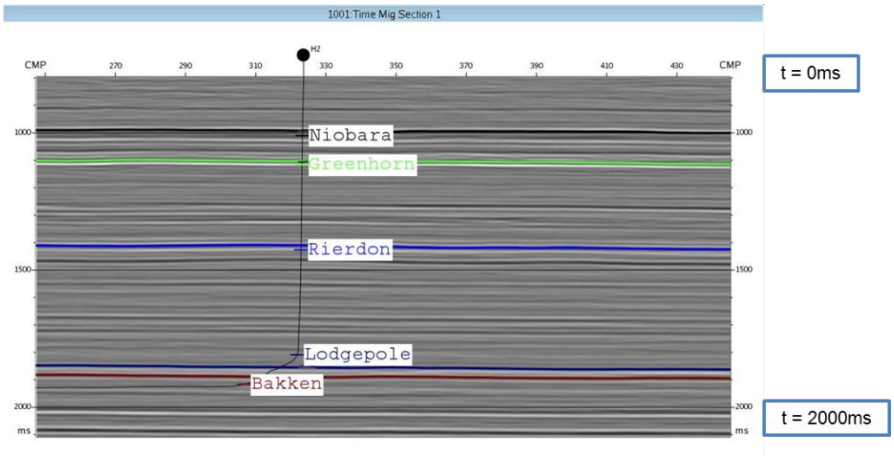

Figure 5.8. Picked horizons/formations on line 1001.

The picked time horizons were gridded within the limit of the user-defined boundary for a quasi-3D time grid. Figure 5.9 shows gridded Niobara Formation picks inside a user-defined boundary. The gridding interpolation algorithm used was the minimum curvature method. The same process was applied to the other seven formations (eight formations in total).

The grids were assigned to individual well markers and they were then calibrated to their assigned markers to check for any mistie. Since mistie can be an indicator for seismic anisotropy, the individual mistie values for each formation at individual well location were recorded.

Figure 5.9 shows a mistie map for the Niobara Formation after calibration to well markers. This same process was repeated for all formations and their assigned

well markers. Figure 5.10 shows the mistie map (and mistie control points) of the same Niobara Formation when compared to well markers. The same process is repeated for all formations and the mistie results are displayed in Table 5.2.

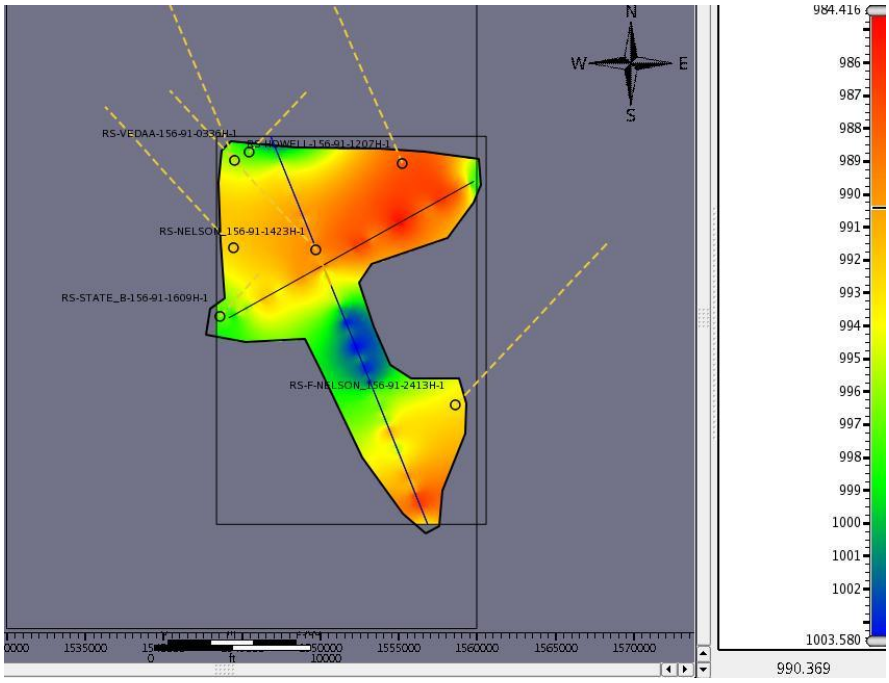

Figure 5.9. Gridded horizon time picks over a user-defined boundary (incorporating all wells) for the Niobara formation.

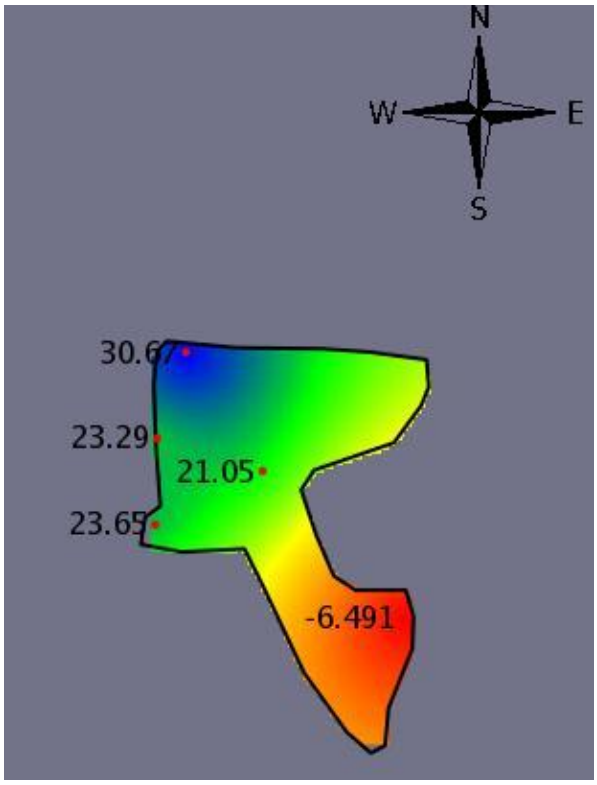

Figure 5.10. Gridded mistie map of Niobara formation (after calibration to well markers); values are in ms.

Table 5.2. Estimated mistie values in ms of all well markers against formations.

Well Name	Niobara Formation (mistie in ms)	Greenhorn Formation (mistie in ms)	Dakota Formation (mistie in ms)	Rierdon Formation (mistie in ms)	Madison Formation (mistie in ms)	BLS Formation (mistie in ms)	Lodgepole Formation (mistie in ms)
RS-STATE	23.65	18.05	-3.38	22.05	5.982	-1.49	-45.84
RS-APELESE	23.29	29.63	8.84	28.70	8.568	6.049	-35.85
RS-VEDAA	30.67					3.318	
NELSON-1423	21.05	18.62	3.334	17.90	0.53	-5.863	-43.57
NELSON 2413	-6.491	-2.181	-15.26	-1.722	-11.71	-17.96	-53.24
RS-BLACKSTONE		25.95	26.15	32.39			-33.75
RS-HOWELL		22.22	0.0469	27.09	6.313	-0.16	-35.73

Conclusion

This thesis gives a meticulous account of all experimental and analytical research work that the author has been involved in during the last two years. Although, they represent individual experiments and studies at different times in the two year MS study program, they are nonetheless related.

The broad aim of this research project broadly has been to observe the seismic response of fractures and relate this to field data. At each stage/chapter, we have discussed different fracture systems and compared them with field-analyzed data. In Chapter 1, we observed that aligned fractures delay seismic velocities especially when transmitting perpendicular to the fracture set. On bigger fractures, this delay is even more pronounced. We had a maximum delay of 5% (equivalent to anisotropic epsilon ε of 0.05) in the larger fractured model. However, seismic wave amplitude increases on entering these fracture zones. This may be due to an increase in elastic scattering or to a higher coda signature. The exact characteristics of these coda signatures are the subject of further research work. In future experimental research study at AGL, these coda signatures will be analyzed to hopefully give more information about the sub-surface. Results from the 3D transmission experiments also revealed that amplitudes increase on arriving at the fracture swarms.

Our investigations to test seismic non-hyperbolic moveout also showed that

residual eta $\boldsymbol{\eta}$ was maximum and more stable when there was a pure VTI symmetry. These tests will be carried out on different fracture orientations and symmetries in the future so as to ascertain which known anisotropic parameters better encapsulates different earth symmetries.

In Chapter 3, we investigated fractures that were much smaller than seismic wavelength. The aim was to look at fracture signatures from the other end of the spectrum and test using the effective medium theories. Stress was also incorporated into the experiment to mimic a real Earth scenario of anisotropic rocks under the influence of pressure from overlying sediments. Phenolic CE which has intrinsic orthorhombic symmetry was used. The experimental study in this Chapter 3 investigated changes in anisotropic parameters and stiffness coefficients in an orthorhombic medium as a function of uniaxial stress. Results showed a maximum increase in compressional and shear wave velocities ranging from 4% to 10% in different directions as functions of increasing uniaxial stress. Compressional and shear wave dependent stiffness coefficients generally increased with stress. Anisotropic parameters (an extension of Thomsen's parameters for orthorhombic symmetry) generally diminished or remained constant with increasing pressure and changes ranged from 0% to 33%. We observed anisotropic behavior a priori to both orthorhombic and VTI symmetries in different principal axes of the model.

This experiment showed that polar anisotropic (specifically VTI) symmetry appear to dominate the character of anisotropy in the Z (or 3) direction as uniaxial

stress increases. This is particularly significant because this direction represents the direction normal to stratification and the plane of most interest to exploration geophysics. However, the orthotropic nature of the composite is revealed in other directions.

We then correlated and related some of our observations to field seismic data. The field data used were the Red Sky 2D seismic data supplied by the Hess Corporation. The field seismic survey was conducted over the Bakken and Greenhorn Formations which are known to exhibit a significant amount of anisotropy due either to the abundance of shales or the presence of aligned cracks. Initial velocity analysis on the 2D data revealed a significant azimuthal bias to the velocity values. Figure 6.1 shows stacking velocities from line 2001 applied to CMP gathers from Line 1001 for NMO correction (and vice versa). It can be observed that these velocities flatten gathers on some horizons and under-correct or over-correct in some others. This is an early indication of azimuthal anisotropy.

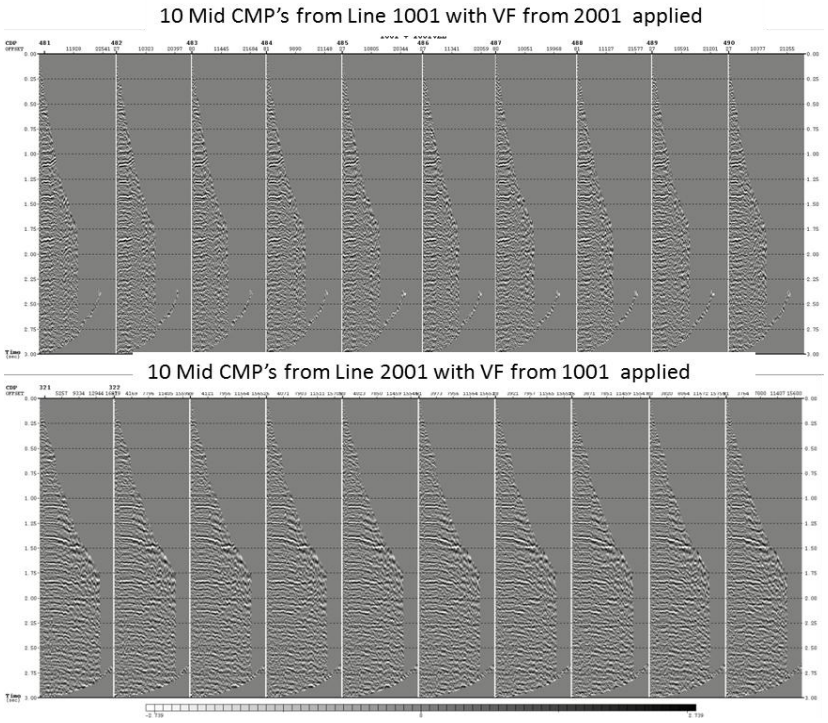

Figure 6.1. NMO corrected CMP gathers. a) 10 mid CMPs from Line 1001 with stacking velocities from Line 2001 applied; b) 10 mid CMPs from Line 2001 with stacking velocities from line 1001 applied (reverse case for {a}).

Vertical functions (time-velocity pairs) for both lines 1001 and 2001 also confirmed this azimuthal bias. Figure 6.2 shows vertical functions averaged over both Lines 1001 and 2001.

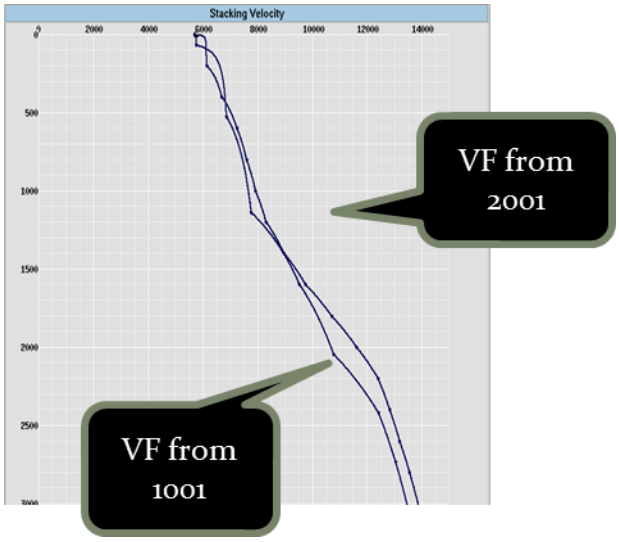

Figure 6.2. Averaged vertical functions (time-velocity pairs) from Lines 1001 and 2001 showing difference in velocity trend.

Significant seismic non-hyperbolic moveout was also observed on both 2D lines. The magnitude of the residual eta $\boldsymbol{\eta}$ at the Greenhorn Formation could be related directly to the eta $\boldsymbol{\eta}$ derived from earlier publications by Jones and Wang (1981). Residual eta results obtained from velocity analysis correlate significantly with values from previous core shale measurements from the Greenhorn Formation.

Earlier experimental results also suggested that higher and more stable residual eta $\boldsymbol{\eta}$ values are likely to occur in a purely VTI medium. If our experimental results are to be related directly to this case, we could say the Greenhorn Formation has VTI symmetry. This is of course most likely the case from previous publications and core shale measurements.

However, of paramount concern is the productive Bakken Formation. From experiments on glass models, we observed that eta values are lower and less reliable when not a perfect VTI medium. Model C9 had lower residual eta readings than Model C10 (Chapter 1).

These experimental approaches to fracture detection and consequent relation to field data are not supposed to be a sort of direct hydrocarbon indicator nor are they exactly indicative of fracture orientation and aperture. Certain assumptions are made when constructing these models and the true geometry of fractures in the subsurface can be much more complicated. Our work however represents a new approach to the problem of imaging fracture swarms. Numerical modeling of complex fracture systems can be difficult but seismic measurement on scaled models can help solve these problems accurately and comprehensively.

Appendix A

Fundamentals of acoustic scattering and seismic anisotropy

1.1 Fundamentals of acoustic scattering and analysis of seismic coda energy

The understanding of scattering characteristics due to fractures is important for reservoir description. When seismic wavelength is large relative to fracture size, the seismic data will be mildly affected by the fractures, and effective medium theories can be used to adequately describe wave motion in such media. The effective medium theory is a theoretical model that allows the prediction of the properties of a heterogeneous medium by replacing small scale heterogeneities with a conceptually homogeneous medium that all the same can predict wave propagation through the heterogeneous medium.

Aki (1969) observed that the power spectra of coda waves from local earthquakes appear to be independent of epicentral distance. The coda waves were as a result of backscattering due to inhomogeneities within the earth crust. He expressed the power spectrum of a coda wave as a function of the earthquake source parameter and a seismic coda propagation term:

$$P(w|t) = |S(w)|^2\, C(w|t)$$

where $P(w|t)$the power spectrum of the coda is waves, $S(w)$ is the earthquake source parameter, and $C(w|t)$ is the coda wave propagation term.

Aki and Chouet (1975) treated high frequency scattering from local earthquakes in central California and western Japan as statistical problems. They also added that the power spectra of different local earthquakes decayed with time and this decay was also independent of epicentral distance. The found this time decay of earthquakes was also independent of the magnitude of the earthquake for earthquakes with a magnitude of less than 6 (Aki, 1969). The coda excitation depended heavily on local geology; it was 5 to 8 times larger in sedimentary rocks than in granite (Aki, 1969). Aki and Chouet (1975) proposed two extreme models to characterize coda wave propagation. The single scattering model assumes each wavelet is due to a single scatterer and that the scattering is weak. This model violates the law of conservation of energy because energy loss in the coda wave is neglected. The second model is the diffusion model and this considers the seismic energy transfer as a diffusion process (Aki and Chouet, 1975). In this model, the law of conservation of energy is obeyed. Considering the single scattering model, the power spectrum of scattered seismic energy can be written as a function of the Fourier transform of the displacement due to backscattering:

$$P(w|t)\Delta t \;=\; |\phi(w\,|\,r)|^2 \;\; 4\sigma\pi r^2 \Delta r$$

where $\phi(w|r)$ is the Fourier transform of a displacement due to backscattering from a single scatterer located at distance r and $\boldsymbol{\sigma}$ is the scattering density (scattering per unit volume). The generalized equation for single scattering theory is as follows:

$$P(w|t) = \frac{v}{2}\, g(\pi) \left| \phi\left(w|\frac{vt}{2}\right)\right|^2$$

where $g(\pi)$ is the backward turbidity coefficient and it is a function of the fractional loss of energy by scattering and v is the propagation velocity.

In the diffusion model, the total seismic energy per unit volume is a function of diffusivity and the intrinsic quality factor Q (this does not include loss due to scattering):

$$\frac{\partial E}{\partial t} = D\nabla^2\, E - \frac{w}{Q}E$$

where $E(x,t,w)$the seismic energy per unit volume within a frequency bound is w, D is the diffusivity and Q is the intrinsic quality factor.

Wu and Aki (1985) proposed a full elastic wave solution to the scattering problem. They derived an expression for Rayleigh scattering using the born approximation approach. For arbitrary heterogeneity with the following parameters, they proposed:

$$\rho(x) = \rho_0 - \delta\rho(x)$$

$$\lambda(x) = \lambda_0 - \delta\lambda(x)$$

$$\mu(x) = \mu_0 - \delta\mu(x)$$

They also suggested the displacement U as the sum of primary wave U^0 and scattered wave U^1:

$$U = U^0 + U^1$$

The force moment tensor M_{ik} of the equivalent point source is

$$M_{ik} = \int_r Q_i X_k \, dV = -\delta_{ik} \overline{\delta\lambda} \, V\nabla . U^0 (X_0) - \overline{\delta\mu} V\left[U^0_{i,k}(X_0) + U^0_{k,i}(X_0)\right]$$

where Q_i is the equivalent body force, V is the volume of the inclusion, $\delta\rho, \delta\lambda$ and $\delta\mu$ are average densities and Lame's constant (Wu and Aki, 1985).

In the early 1990s, the field of time reversed acoustics was introduced by Mathias Fink. Derode et al. (1999) and Fink (2006) demonstrated with the help of piezoelectric transducers that a component after travelling through a highly scattered medium could be reversed and focused to the position of the original source (Figure A1). They demonstrated that wave propagation in a highly scattered medium was repeatable with a high degree of accuracy (Wapenaar et al. 2010).

Snieder et al. (2002) and Gret et al. (2006) exploited the repeatability of the Fink, (2006) experiment and proposed a method called "coda wave interferometry".

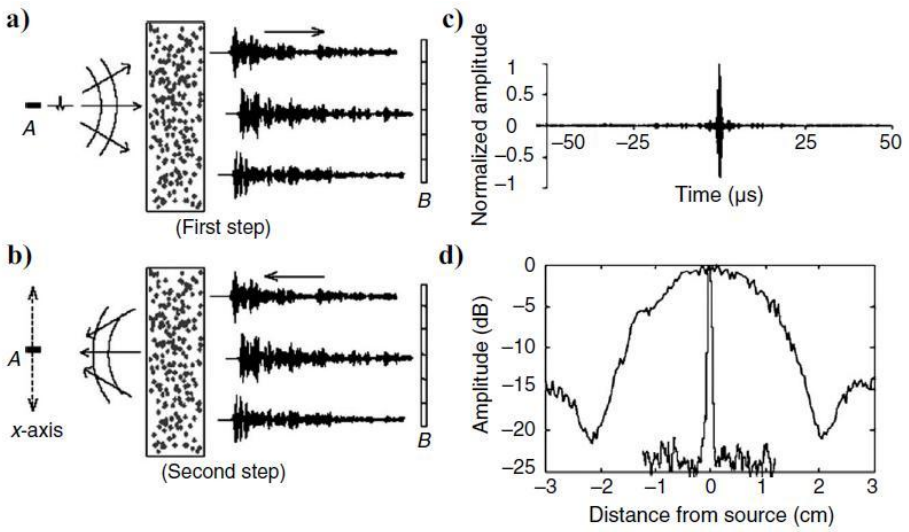

FigureA1.Time reversed acoustics in a strongly scattered medium, Derode et al. (1999); Fink, (2006)

a) Source A emits a pulse that propagates through medium with random scatterer;

b) Array at B emits time-reversed signal that focuses on A after back propagation;

c) Back propagated response; and

d) Beam profile around A.

(modified after Derode et al, (1995); Fink, (2006)

Since Fink's experiment and observations, time-reversed acoustics technology has been used in exploration seismology to back-propagate recorded VSP and surface seismic data to better image complex structures such as faults and salt domes.

1.2 Fundamentals of seismic anisotropy and the effective medium theory

Rock formations are made up of heterogeneities of different scales. These heterogeneities are very often in the atomic scale. They are typically smaller than the wavelength of the incident wavefield travelling through the medium. However, if these heterogeneities are aligned or biased towards a particular direction, then the usual isotropic and homogeneous assumption begins to fail. In essence, anisotropy occurs as a result of aligned inhomogeneities. A fracture or fault with a preferred orientation will give a rock formation an effective anisotropy with a favored axis of symmetry.

Backus (1959) introduced the "equivalent medium theory" to permit the prediction of the stiffness coefficients of a polar anisotropic medium (VTI) from a given set of layers. The equivalent medium theory allows the prediction of properties of a heterogeneous medium by replacing small scale heterogeneities with a conceptually homogeneous medium that can still predict stiffness coefficients from the heterogeneous medium.

Hook's law of elasticity forms the foundation of seismic anisotropy as it does for most of seismology:

$$\tau_{ij} = C_{ijkl} E_{kl}$$

where τ_{ij} is the second rank stress tensor, C_{ijkl} is the fourth rank elastic moduli tensor and E_{kl} describes the strain field.

Consider Newton's equation of motion;

$$\rho \frac{\partial^2 U_i}{\partial t^2} = \frac{\partial \tau_{ij}}{\partial x_j}$$

where U_i is the displacement of a particle at time t and position x and τ_{ij} is the stress tensor (force per unit area) and defining the strain tensor (symmetry of strain tensor)

$$E_{ik} = \frac{1}{2}\left(\frac{\partial U_i}{\partial x_k} + \frac{\partial U_k}{\partial x_i}\right)$$

$$\tau_{ij} = \sum_{k,l} C_{ijkl}\ E_{kl} = C_{ijkl}\, E_{kl}$$

Combine these equations with Hook's law;

$$\rho \frac{\partial^2 U_i}{\partial t^2} = C_{ijkl}\ \frac{\partial^2 U_m}{\partial x_n \partial x_j}$$

We get the generalized wave equation in both the isotropic and anisotropic media.

Hooke's law assumes stress and strain are linearly dependent. As a result,

$$\tau_{11} = C_{1111}E_{11} + C_{1112}E_{12} + C_{1113}E_{13} + \cdots$$

$$\tau_{12} = C_{1211}E_{11} + C_{1212}E_{12} + C_{1213}E_{13} + \cdots$$

The symmetry of the medium is captured in $C_{\alpha\beta}$, since both stress and strain are symmetric i.e., $ij = ji$ (stress symmetry) and $kl = lk$ (strain symmetry); we can simplify using the Voigt notation.

$C_{ijkl} = C_{\alpha\beta}$

ij	11	22	33	23	13	12
α	1	2	3	4	5	6

We can now reconstruct the stiffness matrix as follows:

$$\begin{bmatrix} C_{11} & C_{12} & C_{13} & C_{14} & C_{15} & C_{16} \\ C_{12} & C_{22} & C_{23} & C_{24} & C_{25} & C_{26} \\ C_{13} & C_{23} & C_{33} & C_{34} & C_{35} & C_{36} \\ C_{14} & C_{24} & C_{34} & C_{44} & C_{45} & C_{46} \\ C_{15} & C_{25} & C_{35} & C_{45} & C_{55} & C_{56} \\ C_{16} & C_{26} & C_{36} & C_{46} & C_{56} & C_{66} \end{bmatrix}$$

Once again, due to the symmetry of $C_{\alpha\beta}$, only 21 independent matrix elements are possible.

The types of symmetry available in a crystal depend on the number of independent elastic constants.

Symmetry type	Number of independent elastic constants
Triclinic	21
Monoclinic	13
Orthorhombic	9
Tetragonal	7 (6)
Trigonal (rhombic)	7 (6)
Hexagonal (Polar)	5
Cubic	3
Isotropic medium	2

In this study we have discussed only a few of these symmetries as they affect our experiments and field study.

In an isotropic symmetry, only two independent elastic constants exist and the $C_{\alpha\beta}$ matrix will look like the following matrix:

$$\begin{bmatrix} c & \lambda & \lambda & 0 & 0 & 0 \\ \lambda & c & \lambda & 0 & 0 & 0 \\ \lambda & \lambda & c & 0 & 0 & 0 \\ 0 & 0 & 0 & \mu & 0 & 0 \\ 0 & 0 & 0 & 0 & \mu & 0 \\ 0 & 0 & 0 & 0 & 0 & \mu \end{bmatrix}$$

where $\lambda = c - 2\mu$, $c = K + \frac{4}{3}\mu$ and $\mu = \rho V_s^2$

1.2.1 Polar anisotropy

Polar anisotropy is the simplest realizable anisotropic symmetry in the earth (Ikelle and Amundsen, 2005). It is also commonly known as TI (Transverse Isotropy) symmetry. The symmetry axis is determined by either gravity (VTI) or regional (HTI) stress.

The stiffness tensor of a VTI matrix is as follows:

$$\begin{bmatrix} C_{11} & C_{12} & C_{13} & 0 & 0 & 0 \\ C_{12} & C_{11} & C_{13} & 0 & 0 & 0 \\ C_{13} & C_{13} & C_{33} & 0 & 0 & 0 \\ 0 & 0 & 0 & C_{44} & 0 & 0 \\ 0 & 0 & 0 & 0 & C_{44} & 0 \\ 0 & 0 & 0 & 0 & 0 & C_{66} \end{bmatrix}$$

where $C_{12} = C_{11} + 2C_{66}$

In 1986 Leon Thomsen introduced the Thomsen parameters assuming weak elastic anisotropy. These parameters for a VTI case are summarized here:

$$\varepsilon = \frac{C_{11} - C_{33}}{2C_{33}}$$

$$\gamma = \frac{C_{66} - C_{44}}{2C_{44}}$$

$$\delta = \frac{(C_{13} + C_{44})^2 - (C_{33} - C_{44})^2}{2C_{44}}$$

Epsilon Ɛ is a measure of compressional wave anisotropy, Gamma $\boldsymbol{\gamma}$ is the measure of delay between fast and slow shear waves (will be zero in VTI symmetry) and Delta $\boldsymbol{\delta}$ is a combination of stiffness coefficients and velocities specifically applicable to the field of exploration seismology.

Tariq Alkhalifah (1997)suggested that VTI media had non-hyperbolic moveout and that this moveout was highly dependent on V_{nmo} and η where eta η is a combination of anisotropic parameters and is also a function of horizontal and NMO velocities Alkhalifah, (1997):

$$\eta = \frac{1}{2}\left(\frac{V_h^2}{V_{nmo}^2} - 1\right) = \frac{\varepsilon - \delta}{1 + 2\delta}$$

The hyperbolic travel time equation can therefore be re-written in a non-hyperbolic form:

$$t^2 = t_0^2 + \frac{X^2}{V_{nmo}^2} - \frac{2\eta X^4}{t_0^2 V_{nmo}^4}$$

1.2.2 Orthorhombic Anisotropy

Vertical fractures and horizontal layering combine to form orthorhombic symmetry (Schoenberg and Helbig, 1997). In essence a combination of parallel vertical fractures due regional stress and a background VTI medium is a common cause of orthotropic symmetry. Orthorhombic symmetry is characterized by three

planes of symmetry. Due to two very common geologic phenomena (sedimentation/layering and regional stress), orthorhombic anisotropy might be the simplest and most realistic earth model for any geophysical problem (Schoenberg and Sayers, 1995).

In orthorhombic symmetry the matrix $C_{\alpha\beta}$ has only 9 independent elements:

$$\begin{bmatrix} C_{11} & C_{12} & C_{13} & 0 & 0 & 0 \\ C_{12} & C_{22} & C_{23} & 0 & 0 & 0 \\ C_{13} & C_{23} & C_{33} & 0 & 0 & 0 \\ 0 & 0 & 0 & C_{44} & 0 & 0 \\ 0 & 0 & 0 & 0 & C_{44} & 0 \\ 0 & 0 & 0 & 0 & 0 & C_{66} \end{bmatrix}$$

In 1997, Ilya Tsvankin extended Thomsen's parameters for orthorhombic symmetry. Since there are three mirror symmetry planes, all anisotropic parameters are in triplicate:

$\varepsilon^1 = \frac{C_{22} - C_{33}}{2C_{33}}$	$\varepsilon^2 = \frac{C_{11} - C_{33}}{2C_{33}}$	$\varepsilon^3 = \frac{C_{11} - C_{22}}{2C_{22}}$
$\gamma^1 = \frac{C_{66} - C_{44}}{2C_{44}}$	$\gamma^2 = \frac{C_{66} - C_{55}}{2C_{55}}$	$\gamma^3 = \frac{C_{55} - C_{44}}{2C_{44}}$
$\delta^1 = \frac{(C_{23} + C_{44})^2 - (C_{33} - C_{44})^2}{2C_{33}(C_{33} - C_{44})}$	$\delta^2 = \frac{(C_{13} + C_{55})^2 - (C_{33} - C_{55})^2}{2C_{33}(C_{33} - C_{55})}$	$\delta^3 = \frac{(C_{12} + C_{66})^2 - (C_{11} - C_{66})^2}{2C_{11}(C_{11} - C_{66})}$

References

Aki, K., 1969, Analysis of the seismic coda of local earthquakes as scattered waves. Journal of Geophysical Research, **74**, 615-631.

Aki, K., and B, Chouet., 1975, Origin of coda waves: Source, attenuation, and scattering effects J. Geophys. Res. **80**, 3322-3341.

Alkhalifah, T., 1997, Seismic data processing in vertically inhomogeneous TI media. Geophysics, **62**, 662-675

Backus, M. M., 1959, Water reverberations, their nature and elimination: Geophysics. **24**, 233–261.

Cheadle, S., J, Brown., and D, Lawton., 1991, Orthorhombic anisotropy: A physical modeling study. Geophysics, **50**, 1603-1613.

Chopra, S., and K, Marfurt., 2007, Seismic Attributes for prospect identification and reservoir characterization. SEG Geophysical Development Series; no 11.

Dellinger, J, A., and L, Vernik., 1994, Do traveltimes in pulse-transmission experiments yield anisotropic group or phase velocities? Geophysics, **59**, 1774-1779

Derode, A., A, Tourin., and M, Fink., 1999, Ultrasonic pulse compression with one-bit time reversal through multiple scattering. J. Appl. Phys. **85**, 6343-6352

Ebrom, D., and J, McDonald.,1994, Seismic Physical Modeling. Geophysics reprint series; no 15

Fink, M., 2006, Time-reversal acoustics in complex environments. Geophysics **71**, 151-164.

Golden, B., and R, Wiley., 2007, Geometric attribute analysis on a physical model of HTI. M.S. Thesis, University of Houston

Grandi, S., M.E, Willis., D.R Burns and M.N, Toksoz, 2007, Analysis of scattered signal to estimate reservoir fracture parameters. EAGE/SEG Research Workshop, Perugia, Italy: Expanded Abstract

Gret, A., R, Snieder., and J, Scales., 2006, Time-lapse monitoring of rock properties with coda wave interferometry. J. Geophys. Res. **111**, 03305-03305

Hilterman, F., 1970, Three-dimensional seismic modeling. Geophysics, **35**, 1020-1037.

Hudson, J. A., 1981, Wave speeds and attenuation of elastic waves in material containing cracks. Geophys. J. R. Ast. Soc., **64**, 133-150.

Hudson, J. A., and D.M Boore., 1980, Comments on 'Scattered surface waves from a surface obstacle' by J. A. Hudson. Geophys. J. R. Ast. Soc., **60**, 123-127

Hudson, J. A., E, Liu and S, Crampin., 1996, The mechanical properties of materials with interconnected cracks and pores. Geophysical Journal International., **124**, 105-112

Ikelle, L., and L, Amundsen., 2005, Introduction to Petroleum Seismology, Investigations in Geophysics series; no 12.

Jones, L. E., and H. F, Wang., 1981, Ultrasonic velocities in Cretaceous shale from the Williston Basin. Geophysics, **46**, 288-297.

Lynn, H.B., and L, Thomsen., 1990, Reflection shear-wave data collected near the principal axes of azimuthal anisotropy. Geophysics, **55**, 147-156

Mollhoff, M., C, Bean., and P, Meredith., 2009, Rock fracture compliance derived from time delays of elastic waves. Geophysical Prospecting, **10**, 1365-2478.

Mueller, M., 1992, Using shear waves to predict lateral variability in vertical fracture intensity. The Leading Edge **33**, 29-35

Omoboya, B., J. J, de Fegueiredo., N, Dyaur., and R. R, Stewart., 2011, Effect of overburden pressure on anisotropic parameters in a layered orthorhombic medium. 73rd EAGE Conference and Exhibition, Vienna, Austria: EAGE, Expanded Abstract.

Omoboya, B., J. J, de Fegueiredo., N, Dyaur., and R. R, Stewart., 2011, Uniaxial stress and ultrasonic anisotropy in a layered orthorhombic medium. 81st Annual International Meeting, SEG Expanded Abstracts **30**, 2145-2149

Pervukhina, M., and D.N, Dewhurst., 2008, Stress-dependent elastic properties of shales: Measurement and modeling. The Leading Edge, **27**, 772-779.

Pitman, J., L, Price., and J, Lefever., 2001, Diagenesis and Fracture Development in the Bakken Formation, Williston Basin, Implications on Reservoir Quality in the Middle Member. Denver: USGS.

Sayers, C. M., 2005, Seismic anisotropy of shales. Geophysical Prospecting, **53**, 667-676.

Schoenberg, M., 1980, Elastic wave behavior across linear slip interfaces. J. Acoust. Soc. Am. **68**, 1516-1521.

Schoenberg, M., 1983, Reflection of elastic waves from periodically stratified media with interfacial slip. Geophysical Journal International, **31**, 265-292

Schoenberg, M., and C.M, Sayers., 1995, Seismic anisotropy of fractured rock. Geophysics, **60**, 204-211.

Schoenberg, M., and K, Helbig., 1997, Orthorhombic media: Modeling elastic wave behavior in a vertically fractured earth. Geophysics **62**, 1954-1974

Snieder, R., A, Gret., H, Douma and J, Scales., 2002, Coda wave interferometry for estimating nonlinear behavior in seismic velocity. Science **295**, 2253-2255

Sonnenberg, S.A., and A, Pramudito., 2009, Petroleum geology of the giant Elm Coulee field, Williston Basin: AAPG Bulletin, **93**, 1127-1153.

Steiber, S. J., 1970, Pulsed neutron capture log evaluation in the Louisiana Gulf Coast: Society of Petroleum Engineers, 45th Annual Meeting, paper SPE-2961.

Stewart, R. R., N, Dyaur., B, Omoboya., J. J, de Figueiredo., M, Willis., and S, Sil., 2011 Physical modeling of anisotropic domains: ultrasonic imaging of laser-etched fractures in glass. 81st Annual International Meeting, SEG Expanded Abstracts **30**, 2865-2869

Thomsen, L., 1986, Weak elastic anisotropy. Geophysics, **51**, 1954-1966.

Thomsen, L., I, Tsvankin., and M. C, Mueller., 1995, Layer-stripping of azimuthal anisotropy from reflection shear-wave data. SEG Expanded Abstracts 14, 289-292

Tsvanskin, I., 1997, Anisotropic parameters and P - wave velocity for orthorhombic media. Geophysics, **62**, 1292-1309.

Tsvanskin, I., 1997, Reflection moveout and parameter estimation for horizontal traverse isotropy. Geophysics, **62**, 614-629.

Tsvanskin, I., and L. Thomsen., 1994, Non-hyperbolic reflection moveout in anisotropy media. Geophysics, **59**, 1290-1304.

USGS., 2008, US Geological Survey, Petroleum Resources Assessment of the Bakken Formation. Retrieved January 10, 2010, from www.usgs.com

Wapenaar, K., E, Slob., and R, Snieder., 2010, On seismic interferometry, the generalized optical theorem, and the scattering matrix of a point scatterer. Geophysics, **75**, 27-35

Willis, M. E., D. R, Burns., R, Rao., B, Minsley., M. N, Toksöz., and L, Vetri, 2006, Spatial orientation and distribution of reservoir fractures from scattered seismic energy: Geophysics, **71**, no. 5, 043–051

Wu, R., and K, Aki., 1985, Scattering characteristics of elastic waves by an elastic heterogeneity. Geophysics, **50**, 582-595.

Ye, F., R, Tatham., and M, Sen., 2010, Anticipated seismic responses of the Bakken Formation, East Williston Basin, North Dakota. 80th Annual International Meeting, SEG Expanded Abstracts **29**, 343-347

Yuehua, Z., S, Feng., and A, Keiiti., 1991, Scattering wave energy propagation in a random isotropic scattering medium. J. Geophys. Res. **111**, 607-619.